CHARACTERIZATION OF EXTENDED DEFECTS IN HETEROEPITAXY OF GaSb/Si THIN FILMS WITH CONVENTIONAL TRANSMISSION ELECTRON MICROSCOPY

CHARACTERIZATION OF EXTENDED DEFECTS IN HETEROEPITAXY OF GaSb/Si THIN FILMS WITH CONVENTIONAL TRANSMISSION ELECTRON MICROSCOPY

By

STEFFI YEE-MEI WOO, B.ENG.SOCIETY

A Thesis

Submitted to the School of Graduate Studies

In Partial Fulfillment of the Requirements

For the Degree

Master of Applied Science

McMaster University

MASTER OF APPLIED SCIENCE (2011) McMaster University

(Materials Science and Engineering) Hamilton, Ontario

TITLE: Characterization of Extended Defects in Heteroepitaxy of GaSb/Si Thin Films with Conventional Transmission Electron Microscopy

AUTHOR: Steffi Yee-Mei Woo, B.Eng.Society (McMaster University)

SUPERVISOR: Professor Gianluigi A. Botton

NUMBER OF PAGES: xii, 77

Abstract

Research in the area of improving the efficiency and manufacturability of alternative energy technologies has been of high interest due to the growing environmental concerns of energy resources. Group III-antimonide-based compound semiconductors have been sought after as excellent candidates for photovoltaic conversion of infrared radiation, outside the spectral range absorbed by the currently available crystalline Si solar cells. The major challenge is the GaSb/Si interface is highly lattice mismatched, and inherently heterovalent. This leads to a high density of structural defects, many of which have not been investigated fully. Both optical and electrical properties of such heteroepitaxy thin films are strongly dependent on the periodicity of the crystal lattice, and the presence of extended defects cause perturbations in the lattice periodicity. Therefore the nature of such extended defects must be understood, in order to better manipulate the growth process to minimize their presence. This thesis demonstrates that through the use of conventional transmission electron microscopy, further insight can be gained into understanding the origin, distribution, propagation, and interaction of various extended defects. From this, a couple of ways to systematically suppress some of the defects have also been implemented, and the mechanism by which they induce such a suppression is also discussed.

Acknowledgements

First and foremost I would like to thank my supervisor, Dr. Gianluigi Botton, whom I am forever grateful for making this relay race possible. I greatly appreciate his graciously patient mentorship, continuous inspiration, endless support, and helpful discussions. I hope he knows that what he signed up for taking me on as his Ph.D. student as well.

I have been very fortunate to have picked the brains of some of the most genuine, brilliant, and generous individuals while pursuing graduate studies at McMaster University. An infinite amount of gratitude goes out to my group members, past and present, which as a whole have undoubtedly, made my time in the group one most heartfelt. The space in your stomachs that I have borrowed numerous times to store my baked goods, I hope you have realized by now, will never be returned. Special mentions go to Gabriel Devenyi for the countless discussions, no matter how far-fetched they may be; he was always a willing participant to bounce ideas off of. This work would not have been possible, or at least the images not nearly as pretty without his great advice and resourcefulness. Shahrzad Hosseini, Kai Cui and Shahram Ghanad-Tavakoli, whom I am indebted to for their patient guidance in refining my TEM techniques. Sherri Hadian, for her always-charming conversations about all things non-schoolwork, but schoolwork stuff like crystallography and diffraction contrast too. Fred Pearson,

Andy Duft and Wen He Gong from the CCEM for their in-depth knowledge, great sample preparation tips and tricks, and willingness to always lend a helping hand. Dr. John Preston for his constructive discussions, however elusive (in time, location and topic) they may be. Slowly but surely, I will make a believer in the electron source out of him. Dr. Rafael Kleiman for his great ideas and suggestions, and his ability to bring in graduate students and researchers of all different backgrounds together for such an orchestrated project.

Last but not least, I would like to thank my family and friends, who have been a constant source of encouragement and driving force for this work. Ian Sandink for always being my rock to keep me grounded, and Paige Byers for being the closest thing I have to a sister, for just always understanding. Finally, I wish to thank my parents for their moral support, advice, and endless patience. Despite my perpetual answer of "A couple more years." when asked how much more schooling I have left. I have been so blessed to have such wonderful people in my life; I cannot begin to express my deepest gratitude for all their support.

Table of Contents

List of Figures

List of Abbreviations

2DXRD	Two-dimensional X-ray diffraction
AFM	Atomic force microscopy
APB	Anti-phase boundary
APD	Anti-phase domain
BF	Bright-field
CBED	Convergent beam electron diffraction
DF	Dark-field
DI	Deionized
FOLZ	First-order Laue zone
FWHM	Full-width half-maximum
HOLZ	High-order Laue zone
HRTEM	High-resolution transmission electron microscopy
MBE	Molecular beam epitaxy
MD	Misfit dislocation
RHEED	Reflection high-energy electron diffraction
SAED	Selected area electron diffraction
SFE	Stacking fault energy
SLS	Strain-layer superlattice
TEM	Transmission electron microscopy
WBDF	Weak-beam dark-field
XRD	X-ray diffraction
XTEM	Cross-sectional transmission electron microscopy

1. Introduction

In response to the growing demand for energy resources, and the depleting supply of fossil fuels and other natural resources, sustainable technologies of renewable energy have been highly sought after to reduce carbon emissions and resource consumption to cope with the increased power demand. At the forefront of this area has been research related to improving the efficiency and manufacturability of photovoltaics. Commercial cells are typically single junction silicon devices, while higher efficiency multi-junction devices have also been demonstrated from lattice-matched and bandgap-tuned structures grown on expensive germanium substrates. Examples of these multi-junction systems can be determined using the plot in Figure 1.1, such as the triple junction of InGaP/InGaAs/Ge that is lattice matched to Ge. Presently, no material ideally bandgap-matching to Si has been deposited on Si of sufficient quality to achieve adequate device performance.

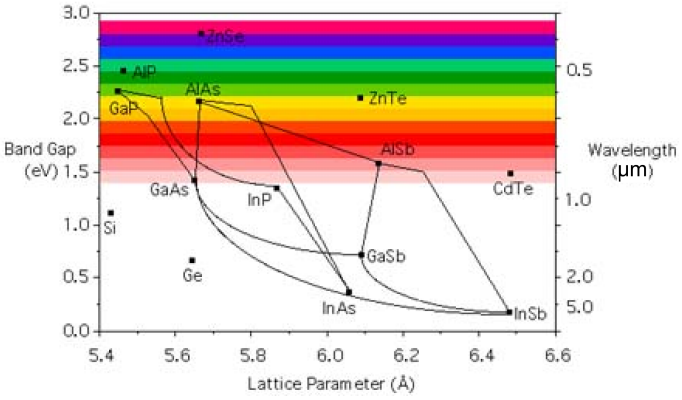

Figure 1.1: The plot of lattice parameters of many common elemental and compound semiconductors as a function of their bandgap energies and complementary wavelength.

Group III-V compound semiconductors can provide several desirable features for optoelectronic device applications, including a wide range of direct bandgaps, and increased carrier mobility. Epitaxial heterostructures of such III-V compounds grown on Si can ultimately increase functionality with the monolithic integration of the III-V devices with the existing Si integrated circuitry technology. This can reduce the overall processing complexity of devices, and hence accelerate their mass production and commercialization.

1.1 Group III-Antimonide Compound Semiconductors

Group III-antimonide-based compounds have been of high interest for a variety of devices such as infrared lasers, high-speed electronics, and photovoltaics. Their bandgap energies range from a narrow 0.17 eV (direct) for InSb, 0.726 eV (direct) for GaSb, to 1.58 eV (indirect) for AlSb. This makes them excellent candidates for photovoltaic conversion of infrared radiation, such as that within the spectral range not absorbed by the currently available crystalline Si solar cells. All group III-Sb compounds exist in a zinc-blende (also known as sphalerite) crystal structure, which is analogous to the diamond crystal structure that group IV elements (such as Si and Ge) adopt. Both structures consist of two interpenetrating face-centred cubic (fcc) sublattices positioned <¼, ¼, ¼> relative to one another, such that each atom within the unit cell is tetragonally coordinated. The zinc-blende structure differs in that the two sublattices are exclusively occupied by one of the group III or V elements; therefore each atom has nearest neighbours of the opposite element. Because of this, the zinc-blende

structure lacks inversion symmetry so the bonds are considered polar, meaning orthogonal directions such as [110] and $[1\bar{1}0]$ are not equivalent and the polarity in the bonding from the group III to the group V element can be designated. Similar to other fcc structures, the {111} planes are the closest packed planes, where the stacking sequence is ABCABC along {111} planes.

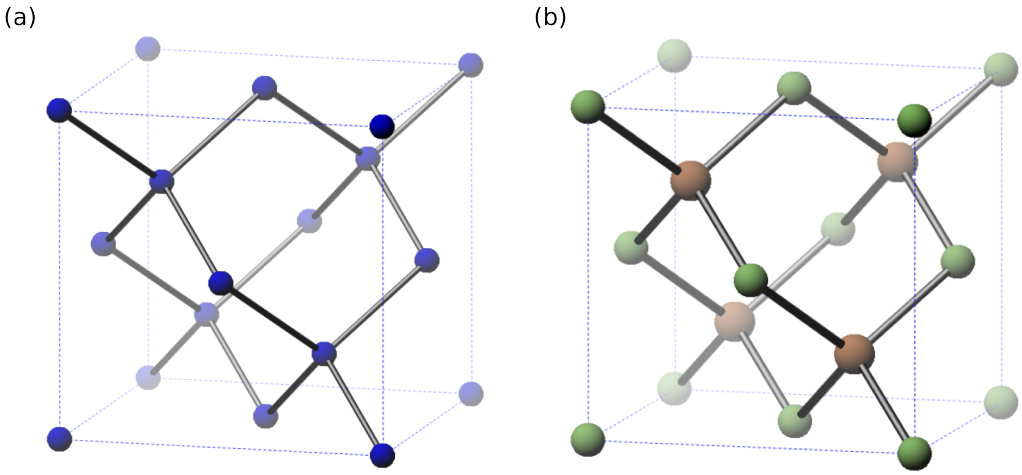

Figure 1.2: Unit cell of (a) diamond-structured Si, and (b) zinc-blende-structured cubic III-V semiconductor, where the generic notation is to place the group III atoms at the cell corners.

1.2 Si(001) Surface

Surface steps on a Si(001) substrate can be classified into two main categories, ones of odd or even number of atomic layers high, or simplified as single steps or double steps, respectively. Because there is significant distinction based on the orientation of the step edge with respect to the direction of the surface dimerization of dangling bonds, there are four different step configurations shown in Figure 1.3. Single steps with step edge parallel (S_B) or perpendicular (S_A) to the dimerization direction on the (top) terrace, and double steps with parallel (D_B) or perpendicular (D_A) to the dimerization direction. Single

step S_A is the simplest structure of the four configurations because of no extra dangling bonds or strain induced by rebonding at step edges (Fang *et al*., 1990), therefore it is the most energetically favourable step in Si(001) (Chadi, 1987; Kroemer, 1987). There is experimental evidence (Fang *et al*., 1990; Kroemer, 1987) that a high temperature treatment of a vicinal Si(001) substrate prior to growth would lead to the reconstruction of alternating single steps of S_A and S_B into double steps D_B, driven by a decrease in formation energy (Chadi, 1987). The understanding of these surface steps is important because the presence of single steps have been attributed to the main cause for anti-phase boundaries (defined later) in growths of GaAs/Si, GaAs/Ge, and GaP/Si.

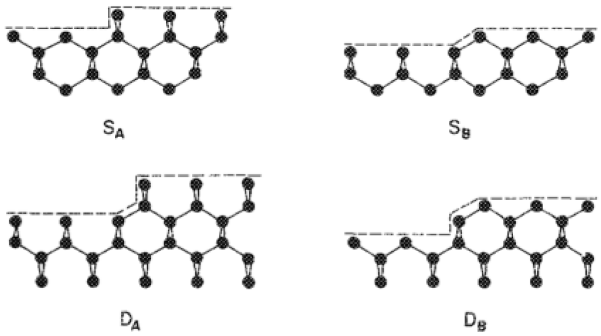

Figure 1.3: The four different step configurations of Si(001) substrates in side view (Fang *et al*., 1990).

1.3 Structural Defects in Epitaxial Growth

One of the biggest challenges in the epitaxial growth of group III-V semiconductors, particularly on non-polar substrates such as Si, are the resulting structural defects. This is mainly due to mismatches in lattice parameters between the substrate and film, as well as mismatches in thermal expansion coefficients that become a larger contributing factor at high growth temperatures. The GaSb/Si

interface with lattice parameters of 6.0959 Å and 5.431 Å, respectively, has a very high lattice mismatch of 12.2%. These defects can be defined in broad classes: strain relief defects such as dislocations, deformation twins, and growth defects such as epitaxial twins and anti-phase boundaries.

1.3.1 Threading and Misfit Dislocations

Linear defects of threading dislocations and networks of interfacial misfit dislocations can arise, as a major mechanism for strain relief in the lattice-mismatched system. The use of vicinal substrates in which the wafer is misoriented from the [001] substrate normal is often suggested to be effective in the minimization of threading dislocation density. Another commonly utilized remedy is the introduction of a strained-layer superlattice, which is known to induce additional strain into the system to bend away propagating dislocations (Fang *et al*., 1990). The compressive strain, which is introduced by a material with a larger lattice constant, repulses the dislocation away from the source of the strain, called the Peach-Koehler force (Cahn, 1963; Fang *et al*., 1990). If the layer thickness of the larger lattice constant material is less than the critical thickness, no additional dislocations are introduced (Fang *et al*., 1990).

1.3.2 Stacking Faults and Microtwins

Most of these extended crystalline defects tend to occur along the closest packed planes of {111}, such as stacking faults, and microtwins. Stacking faults are interruptions in the ABCABC stacking order in the {111} planes. Initiated by the dissociation of a perfect dislocation with Burgers vector **b** = a/2 <110> into

two partial dislocations with Burgers vector **b** = a/6 <112> bounding the resulting stacking fault.

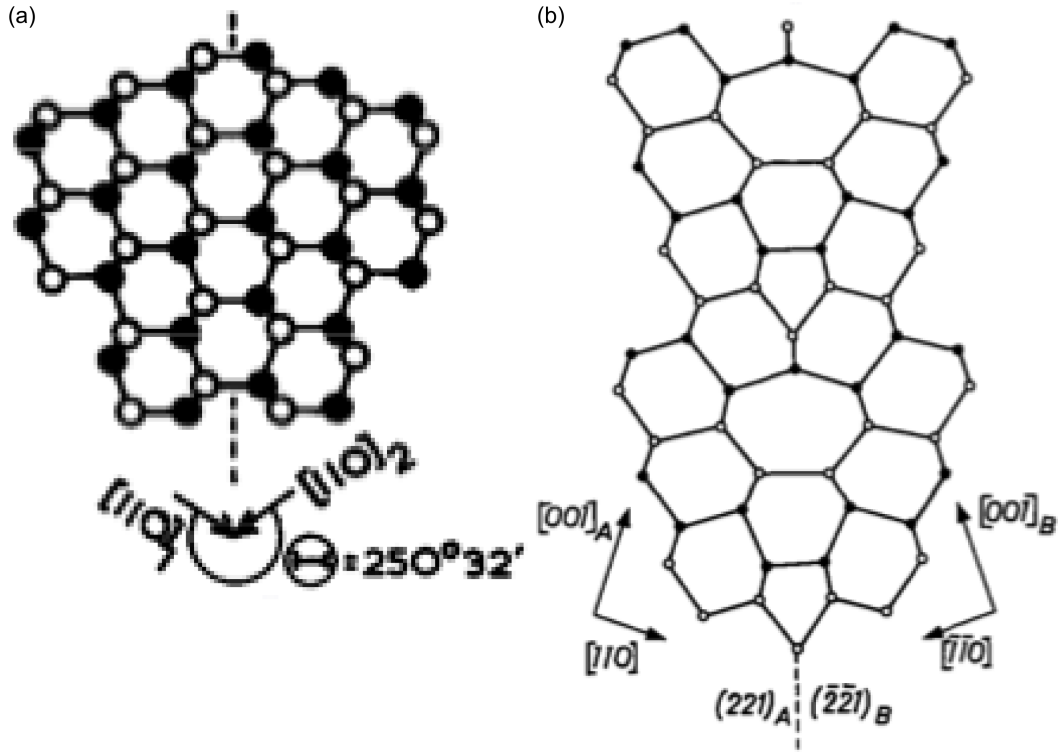

Figure 1.4: Ball and stick model of (a) a {111} twin boundary (dotted line) in zinc-blende structure (Holt, 1969), and (b) one of the two configurations of an incoherent {114} boundary at the intersection of two first-order twins of opposing habit planes in diamond structure (Hornstra, 1959).

Twins are regions of mirrored stacking sequence in the closest packed planes of {111} within the crystal as illustrated in Figure 1.4(a), where each consecutive layer is shifted after the first bounding stacking fault (Wagner, 1966). Epitaxial twins are a far more common planar defect in such heteroexpitaxial structures than those that arise from anti-phase disorder (Ernst & Pirouz, 1989), discussed in the following section. Microtwins have been considered a low-impact defect, due to their unstrained coherent interfaces along {111} planes and lack of dangling bonds. Due to their minor disruption in the crystal symmetry, they are

only expected to have a low density of trapping states (Holt & Yacobi, 2007). Their effect on electrical properties, however, is likely in the form of scattering centres, which reduce mobility (Parkinson *et al*., 2009). However, this view of twins considers them as completely isolated entities in the material, ignoring the fact that microtwins are likely to intersect during growth in epitaxial films. The intersection of twins of different habit planes, as a result, will lead to unsatisfied bonds. For example, first-order microtwins formed on opposing habit planes can terminate from mutual intersection along a {114} plane (see Figure 1.4(b)), which is highly incoherent, resulting in unsatisfied bonds and trapped charge (Hornstra, 1959). Furthermore, twins that intersect from adjacent habit planes will also form incoherent interfaces on high-order planes. Finally, second- and higher-order twinning is expected to create dangling bonds, and will result in further unsatisfied bonds between the twinned regions and epitaxial film.

1.3.3 Anti-Phase Disorder

Unique to the growth of a polar cubic III-V film on a non-polar group IV substrate particularly those that are (001)-oriented, the heterovalent interface is inherently susceptible to anti-phase disorder because of ambiguous nucleation at the substrate surface. This is due to the two equivalent orientations corresponding to the interchange of group III and V sublattices with respect to the two sublattices of Si at the substrate surface. Anti-phase disorder can be explained by the reversal in the atomic constituents in the two sublattices of the unit cell, which

is to say a reversal in crystal polarity, and equivalently a reversal in bond directionality.

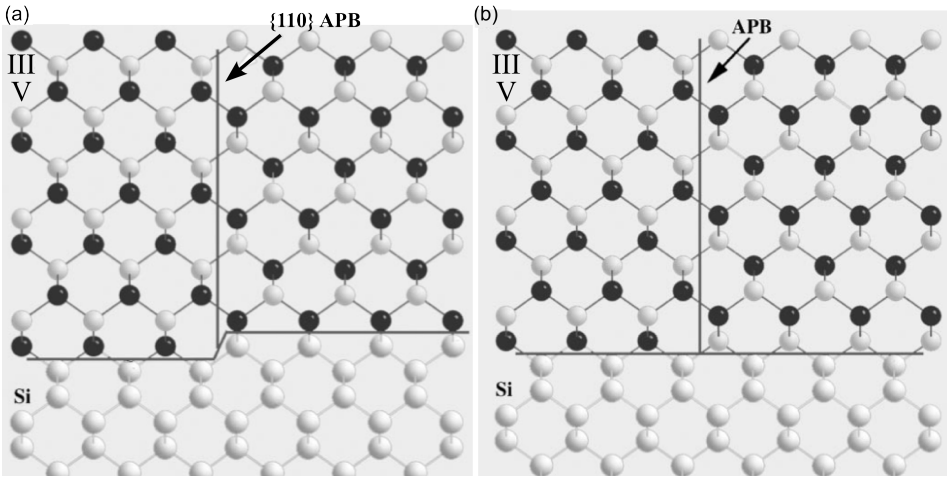

Figure 1.5: Possible origin of an APB along {110} plane, (a) at a single step, (b) due to mixed domain nucleation (Cohen & Carter, 2002).

One possible origin of this is the nucleation of domains of opposite bond directionality at the occurrence of single steps of a/4 in height inherent in the Si substrate (Figure 1.5(a)). This is assuming that an exclusive element is laid down as the first layer species during growth on the step terraces adjacent to this single step. A secondary case is the possibility of nucleating both group III- and group V-prelayer domains on the same terrace (Figure 1.5(b)), which would also cause a reversal in bond directionality. Both cases result in planar anti-phase boundaries (APBs), which consist of wrong III-III and/or V-V bonds separating domains of opposite polarity called anti-phase domains (APDs). The crystal symmetry operation by which an APB occurs is equivalent to an $\boldsymbol{R}$ = a/4 <111> rigid body translation along its plane (Cho, De Cooman, Carter, Fletcher, & D. K. Wagner, 1985), in addition to a 90° in-plane rotation about the substrate normal of [001]

(Cohen & Carter, 2002; Komninou, Stoemenos, Dimitrakopulos, & Karakostas, 1994).

APBs, similar to grain boundaries, perturb the periodicity of the lattice, and therefore share similar electrical and optical properties. The wrong bonds across APBs can result in trapping and scattering of charge carriers (Holt, 1969). APBs as planes of charged structural defects are expected to induce a highly compensated behaviour to the semiconductor electrical properties (Fang *et al*., 1990), or act as non-radiative recombination centres in polar materials such as GaSb (Holt, 1969; Kroemer, 1987). APBs facet parallel to low-order crystallographic planes such as {110}, {111}, {112}, {113}, and possibly even {100} (Cohen & Carter, 2002; Holt, 1969; Kroemer, 1987). Experimental evidence in GaAs/Si, GaAs/Ge, GaP/Si systems report APBs existing along or close to {110} planes from the interface to the film thickness, or as "self-annihilating" APBs that start and end at the interface overgrown by the dominant domain (Georgakilas *et al*., 1993; Kawabe & T. Ueda, 1987; Li & Giling, 1996; Li, Lazzarini, Giling, & Salviati, 1994; O. Ueda, Soga, Jimbo, & Umeno, 1989). As supported by theoretical calculations, {110} planes have the lowest energy of formation (Rubel & Baranovskii, 2009) because APBs of this type are considered stoichiometric for having equal numbers of III-III and V-V wrong bonds.

1.4 Research Objective and Thesis Overview

Given the multitude of defects, from the large lattice mismatch between GaSb thin films grown on Si substrate, the general aim of this research was

therefore to investigate the origin, distribution, and propagation of extended defects in the heterostructures, using conventional transmission electron microscopy techniques.

This thesis consists of six chapters. Chapter 1 provides the introduction of group III-V compound semiconductors, the Si substrate, as well as structural defects that can arise. Chapter 2 involves a literature review, including the usage of AlSb as a buffer layer, previous analysis using transmission electron microscopy, and the techniques to identify one of the most electrically detrimental defect of APBs, as well as a possible solution to minimize their occurrence. Chapter 3 details the experimental methods, including sample preparation details. Chapter 4 provides the results of the experimental studies on the growth and characterization of the GaSb/Si heterostructures; specifically it includes the unambiguous identification of misfit dislocations, microtwins, and APBs. Chapter 5 presents the nature of various extended defects, their interaction and asymmetrical distribution (in some cases), and the possible mechanisms for their reduction. Chapter 6 summarizes with the conclusions and future work.

2. Literature Review

2.1 Heteroepitaxial Growth of III-Sb on Si(001)

One of the first reports of the growth of group III-Sb compound semiconductors on Si(100) is the work of Malik *et al*. (1986). Multilayers of GaSb/AlSb were grown by molecular beam epitaxy (MBE), while the film nucleation was investigated with in-situ reflection high-energy electron diffraction (RHEED), studying the evolution of the RHEED pattern during various stages of growth. The film morphology has always been an area of interest, and was demonstrated using Normarski interference microscopy and TEM. At the time, such heterostructures were not of the utmost crystalline quality.

2.1.1 AlSb as Buffer Layer

In order to improve the quality of the films, the use of AlSb as a buffer layer during the growth of GaSb by MBE was first proposed by Akahane *et al*. (2004), based on results from X-ray diffraction (XRD) rocking curves. Through the minimization of the full-width half-maximum (FWHM) of the (004) reflection perpendicular to the substrate, the thickness of the buffer layer and growth temperature were optimized. The smaller the FWHM of the (004) reflection, the lower the degree of misorientation in that direction within the epilayer. The FWHM of the XRD rocking curve plotted as a function of AlSb thickness with growth temperature fixed at 500 °C is shown in Figure 2.1(a). The dependence of

the FWHM of the XRD rocking curve with growth temperature for a 10 nm thick AlSb layer is shown in Figure 2.1(b).

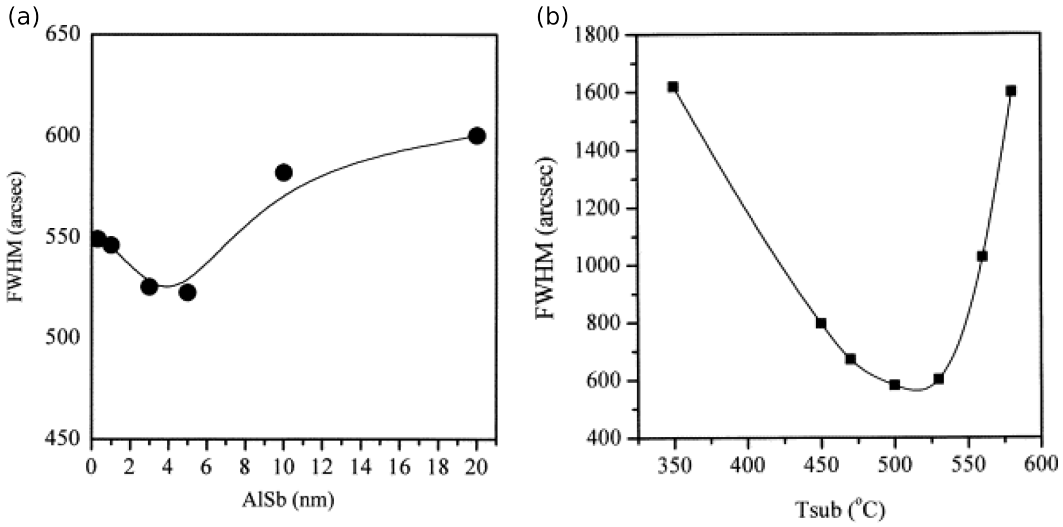

Figure 2.1: Dependence of FWHM of XRD rocking curve on (a) the thickness of AlSb layer with growth temperature fixed at 500 °C, (b) the growth temperature with 10 nm AlSb layer (Akahane, Yamamoto, Gozu, & Ohtani, 2004).

Through these results, it was demonstrated that the FWHM is lowest for a buffer layer thickness of 5 nm. However only 1 monolayer is sufficient in drastically decreasing the FWHM while eliminating the cloudy GaSb surface common in the samples without any AlSb layer. From this, Akahane *et al*. (2004) also surmised that the role of AlSb as a buffer layer in improving the crystal quality of GaSb is its surfactant behaviour on the Si substrate. Additionally, a spotty RHEED pattern during the growth of the buffer layer indicates three-dimensional nucleation or island growth, which can aid to prevent the generation and propagation of dislocations at the interface.

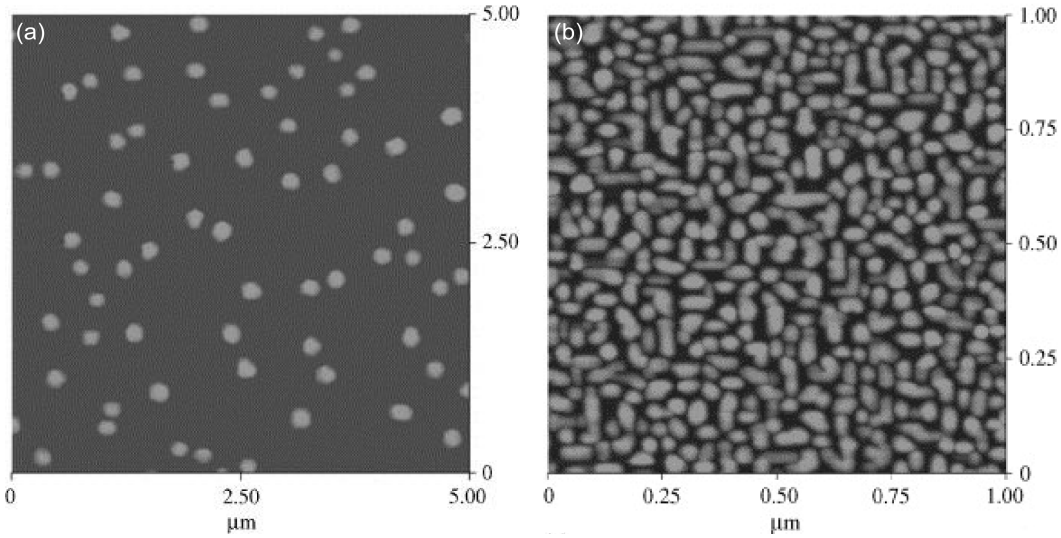

Figure 2.2: AFM images of 5 nm of GaSb (a) without and (b) with 5 nm AlSb buffer layer. Please note the change in length scale between the two images (Akahane, Yamamoto, Gozu, Ueta, & Ohtani, 2005).

The surface morphology of such AlSb buffer layers during the initial stages of growth on Si(001) became an area for further investigation. An atomic force microscopy (AFM) image of a 5 nm layer of AlSb shows that they form small islands (~ 25 nm in diameter) in high density, and 5 nm of GaSb grown thereafter is shown in Figure 2.2(b). In comparison, a 5 nm layer of GaSb form islands about 10 times larger in much lower density, as shown in Figure 2.2(a).

2.2 TEM Characterization of GaSb Heterostructures

Transmission electron microscopy (TEM) techniques have been a vital tool in the investigation of the defect structure in GaSb thin films grown on Si substrates. For example, conventional TEM was used to semi-quantitatively determine the dislocation density as a function of GaSb film thickness (Akahane, Yamamoto, Gozu, Ueta, & Ohtani, 2006). TEM is also one of few techniques capable of studying the GaSb/Si interface, as well as the boundaries of coalescing

GaSb islands. Using a combination of high-resolution TEM (HRTEM) and selected area electron diffraction patterns, Kim *et al*. (2006) were able to identify twin boundaries, and the orientation relationships between the regions separated by these boundaries and the Si substrate.

Interfacial misfit dislocations (MDs) have been extended defects of high interest, due to their role in the strain relaxation of the epilayer. Due to the very large lattice mismatch between GaSb and Si (12.2%), the MDs observed are almost exclusively 90° dislocations (also known as Lomer dislocations or perfect dislocations) (Kim *et al*., 2006; Vajargah *et al*., 2011). With a Burgers vector of **b** = a/2 <110>, the projected edge component onto the interface makes 90° dislocations twice as effective at misfit relaxation than 60° dislocations (Kim *et al*., 2006). Similarly in the AlSb/Si system (with an even larger 13.0% lattice mismatch), 90° dislocations also dominate as the major type of MDs in the array at the interface, as demonstrated in HRTEM images by Huang *et al*. (2008) in Figure 2.3(a).

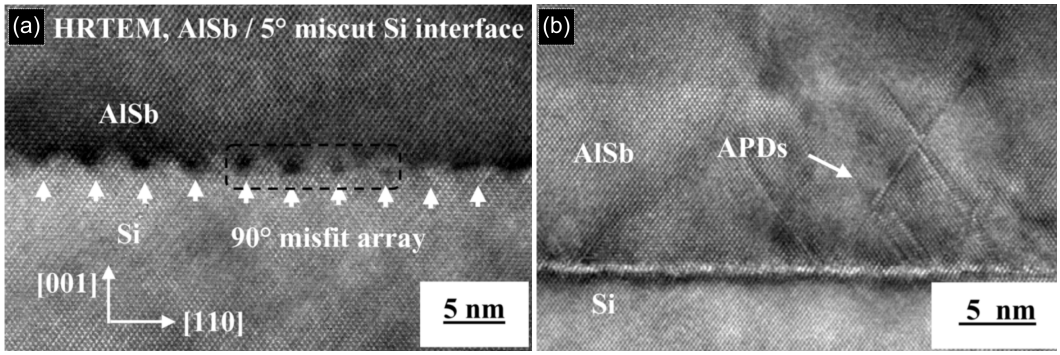

Figure 2.3: HRTEM image of the <110> cross-section showing (a) an array of 90°misfit dislocations, (b) the first report of APDs in Sb-based compounds grown on Si (Huang, Balakrishnan, Khoshakhlagh, Dawson, & Huffaker, 2008).

In this same work, Huang *et al*. also reported the presence of anti-phase domains (APDs), a first in the growth of Sb-based compounds on Si substrates. As shown in Figure 2.3(b), these defects, identified by the authors as APDs, are bounded by APBs lying on {111} planes. However, no further details were reported regarding how or whether a reversal in polarity was confirmed. Therefore it is highly likely that these planar defects lying on {111} planes seen edge-on in this cross-section, are actually microtwins that have been misidentified as APBs. One major reason for such an assumption is the MBE growth process highly favours stoichiometry. While APBs that lie on {111} planes will be made up of exclusively wrong III-III or V-V bonds, therefore the stoichiometric tendencies in the MBE growth process would not be satisfied.

2.3 Detecting Anti-Phase Domains with Superlattice Reflections

APDs are detectable through techniques such as anisotropic chemical etching (Li & Giling, 1996; Morizane, 1977; Uppal & Kroemer, 1985), XRD (Neumann, Zabel, Fischer, & Morkoç, 1987), Raman Scattering (Fischer *et al*., 1985), RHEED monitoring (Uppal & Kroemer, 1985), and TEM (Gowers, 1984; Li *et al*., 1996; Liliental-Weber, Weber, Parechanian-Allen, & Washburn, 1988). Advantages of detecting APBs with conventional TEM highlight the limits of the other two commonly used techniques: XRD, which characterizes the spreading in the scattering of superstructure peaks, and anisotropic etch. Both techniques rely on APDs contributing to a substantial fraction of the film surface, and are limited to domain sizes larger than 200 nm and 400 nm, respectively (Fischer *et al*., 1985;

Neumann *et al*., 1986). The broadening theory behind the XRD technique suggested by Neumann *et al*. (1987) requires the APDs and the in-phase domains to be striated perpendicular to the interface as measured by reflections along that surface normal. However, experimental evidence of APBs and their respective APDs (Cho & Carter, 2001; Georgakilas *et al*., 1993; Hudait & Krupanidhi, 2000; Kawabe & Ueda, 1987; Liliental-Weber *et al*., 1988) mostly do not exist in this type of geometry.

Superlattice imaging in cross-sectional TEM is able to reveal both the APBs that propagate to the film surface, as well as those of self-annihilating nature. This type of diffraction condition has been used to observe APBs in ordered fcc alloys (e.g. Cu_3Al), and the invisibility criterion ($\mathbf{g}.\boldsymbol{R} = 0$) notes that APBs are only visible with superlattice reflections as ribbon-like boundaries, and not with fundamental reflections (Edington, 1976; Loretto, 1994). The amplitudes of opposite superlattice reflections are not equal, as demonstrated with *200* and *-200* reflections for APBs in tetragonal systems (e.g. rutile), which have fringe characteristics. Under *g* and *-g* images formed with superlattice reflections, the contrast of those fringes is reversed (van Landuyt, 1966), as demonstrated in Figure 2.4.

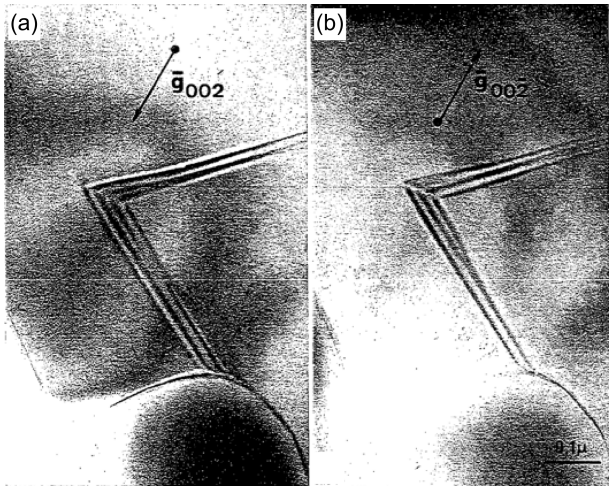

Figure 2.4: An APB in rutile (tetragonal crystal structure) showing a reversal in fringe contrast between images formed with opposite superlattice reflections (van Landuyt, 1966).

Superlattice reflections, such as those of *200*-type are particularly sensitive to changes in the chemical nature of the occupants of the two sublattices in the zinc-blende structure. This is due its structure factor (F_{hkl}) as shown in equation (2.1). For the permitted reflections when h, k, l are all even, and $(h + k + l) = 4n + 2$, it is proportional to the difference in atomic scattering factor (f) of the two occupants in the sublattices as shown in Equation (2.2) (Gowers, 1984). Such superlattice reflections are kinematically forbidden in the diamond structure.

$$F_{hkl} = \{f_{III} + f_V \exp[\frac{\pi}{2} i(h + k + l)]\} F_{fcc} \tag{2.1}$$

Because of this, it can be used to reveal interruptions in atomic ordering when the contrast of these *200*-type reflections is exclusively isolated, such as under two-beam dark-field diffraction condition (Posthill, Tam, Das, Humphreys, & Parikh, 1988). A superlattice bright-field diffraction condition on the other hand, is strongly affected by sample thickness variation.

$$F_{hkl} = 4\{f_{III} - f_V\} \tag{2.2}$$

2.3.1 Convergent Beam Electron Diffraction for Crystal Polarity

In zinc-blende structures, it is expected that across an APB, a relative rotation of $\pi/2$ in the adjacent domains exists about the substrate surface normal of [001], which is equivalent to the reversal in crystal polarity (bond directionality). This can be confirmed by the convergent beam electron diffraction (CBED) technique prescribed by Taftø and Spence (1982) to determine (absolute) crystal polarity. Determining the polarity means identifying the directions pointing from the group III cation to the nearest neighbour group V anions, or vice versa, also known as the $<111>_A$ – $<111>_B$ direction (Spiecker, 2002). This technique requires the simultaneous coupling of a superlattice reflection, *200* for example, with two weak first-order Laue zone (FOLZ) odd-indexed reflections at Bragg condition. An example of a possible scattering path is shown in Figure 2.5, where the path from the central beam to the superlattice reflection through the two odd-indexed FOLZ reflections is outlined. This is typically done by tilting far away (close to 10º) from a <011> zone axis, and is comparable to achieving a dark-field diffraction condition.

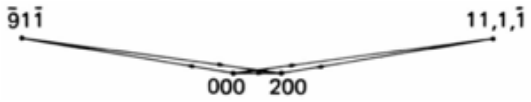

Figure 2.5: Schematic showing the scattering path from the 000 central beam to the 200 superlattice reflection, bypassing the two FOLZ reflections ($\bar{9}1\bar{1}$ and $11\,1\bar{1}$) (Taftø & Spence, 1982).

This technique can be used to determine polarity of non-centrosymmetric crystal structures, because during strong multiple scattering of weak beams, Friedel's law breaks down. This breakdown, due to a lack of mirror symmetry

parallel to the (200) plane, can be detected by interpreting the contrast of the dynamically interacted Bragg lines crossing in the dark-field superlattice diffraction disc (Ishizuka & Taftø, 1984). The constructive interference of this type of scattering results in FOLZ lines with bright contrast called excess lines; the corresponding destructive interference results in FOLZ lines with dark contrast called deficient lines, as shown in Figure 2.6.

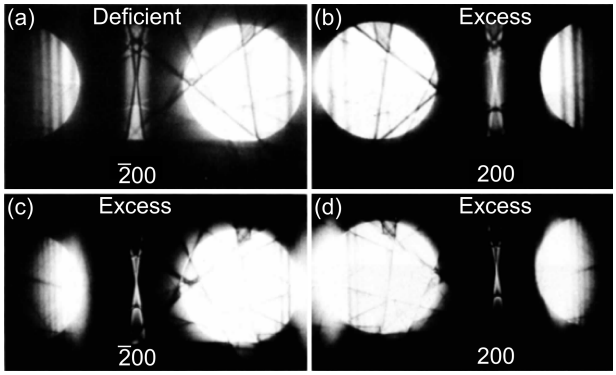

Figure 2.6: Examples of the CBED diffraction condition, in (a, b) GaAs and (c, d) Ge, which are non-centrosymmetric and centrosymmetric, respectively (Taftø & Spence, 1982).

Experimental TEM observations of APBs show that they may be curved and ribbon-like, or faceted parallel to various low-order crystallographic planes such as {110}, {112}, {111}, {113}, or even {100} (Cohen & Carter, 2002; Holt, 1969; Kroemer, 1987). The faceting nature is most likely driven by the minimization of interfacial energy, in order to maintain the stoichiometry, which is encouraged during MBE growth. This is demonstrated by the cross-sectional superlattice dark-field image (a), as well as the plan-view bright-field image (b) of Figure 2.7.

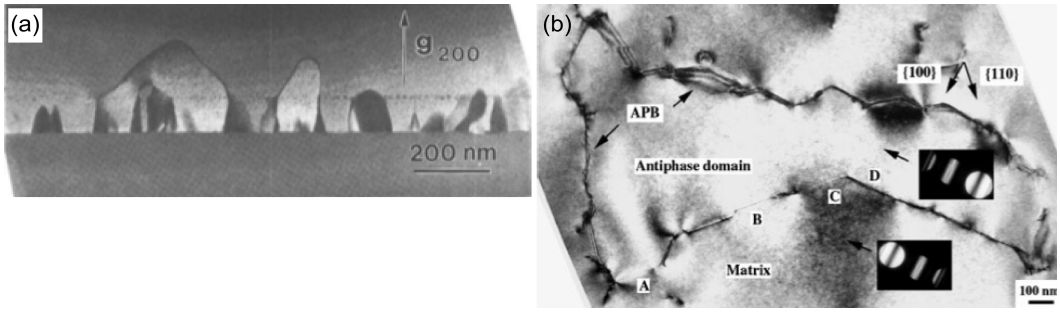

Figure 2.7: (a) Cross-sectional DF image of self-annihilated APBs in GaAs/Ge (Guelton, Saint-Jacques, Lalande, & Dodelet, 1995), (b) Plan-view BF image of an APD in which the CBED technique by Taftø and Spence (1982) confirms the reversal in polarity (Cohen & Carter, 2002).

In Figure 2.7(b), the CBED technique by Taftø and Spence (1982) is used to confirm the presence of a reversal in crystal polarity. A reversal in polarity in the domain separated by the close-looped ribbon-like boundary would cause a π-phase change in the FOLZ contribution. The contrast of the crossing in the superlattice diffraction disc obtained from the region labeled "Antiphase domain" is observed to be the same as the contrast of the crossing in the opposite superlattice diffraction disc obtained from the region labeled "Matrix" (Cohen & Carter, 2002). This is indicative of an interchange of the $\{111\}_A$ and $\{111\}_B$ faces between the two regions, meaning a reversal in the polar bond directionality, therefore the planar defects separating them can be concluded as being APBs.

Compound semiconductors like GaSb (Z = 31, 51) that have a large difference between their atomic scattering factors (*f*), as compared to GaAs (Z = 31, 33) that only has a small difference, can cause two major effects in the CBED pattern for GaSb. Firstly, the intensity of the *200*-type reflection is much stronger, so dynamical scattering comes into play at smaller sample thicknesses. This is because the intensity is proportional to the square of the structure factor (F_{hkl}),

which is related to the difference between the atomic scattering factors, as shown in Equation (2.2). Secondly, the interference of the scattering path from *000* → *hkl* → *200* is not as effective as in GaAs, so the structure amplitude deviates from ±π/4, and the excess lines are affected, becoming less strong. These two factors contribute together to increase the difficulty in distinguishing constructively interfered excess lines. Simulated intensity distributions comparing the *000* BF disc and the {*200*} DF discs for CBED for GaAs and GaSb has been done by Spiecker (2002) to demonstrate these effects, as shown in Figure 2.8.

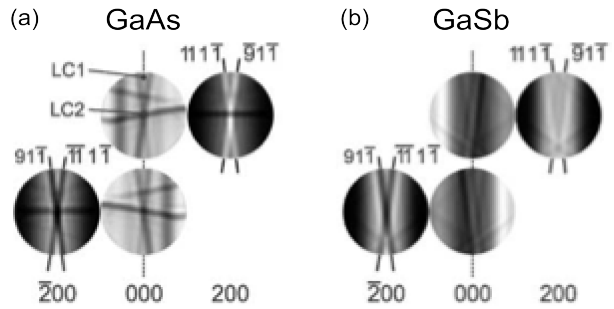

Figure 2.8: Simulated intensity distributions of the 000 disc and {200} DF discs for CBED near the [011] zone axis of (a) GaAs, and (b) GaSb, of a 100 nm thick crystal slice (Spiecker, 2002).

2.4 The (211)-oriented Si Substrate Proposition

One of the solutions to minimizing the occurrence of APDs is to grow on a Si surface that can offer two energetically non-equivalent sites to accommodate the nucleation of both the group III and group V elements, as suggested by Kroemer *et al*. (1987). The (211)-oriented Si surface is the simplest truncated surface that satisfies that criteria without the need for surface rearrangement, as well as the interface neutrality condition of $h \pm k \pm l = 0$.

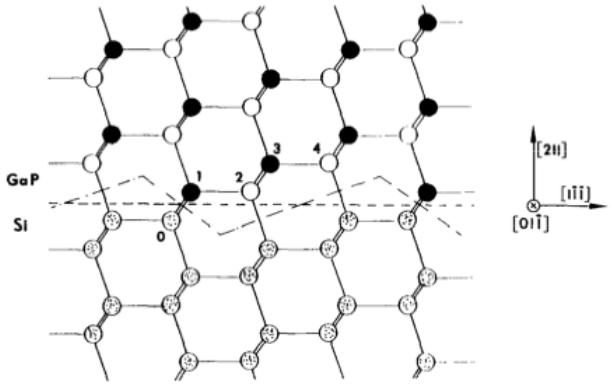

Figure 2.9: Atomic arrangement of an idealized cubic III-V semiconductor/Si(211) interface. Each III-V plane parallel to the interface has equal number of III and V atoms and is hence electrically neutral (Kroemer, 1983).

The Si(211) plane is an intrinsically stepped surface with two non-equivalent sites corresponding to the two sublattices in the Si diamond structure, made up of two terrace atoms (white sublattice sites in Figure 2.9) and one edge atom (black sublattice sites in Figure 2.9) with one and two dangling bonds respectively. Because of this, group III and group V atoms are expected to register exclusively at one of the two sites from the Si substrate. Therefore a Si(211) substrate is expected to provide a surface that induces growths of III-V heteroepitaxy where atomic III-V planes parallel to the interface has equal numbers of group III and group V atoms, as shown in the schematic in Figure 2.9. This is the nature of the interfacial electrical neutrality. Both of these qualities will contribute to eliminating the heterovalency problem inherent in the growth of polar on non-polar materials, in order to reduce the occurrence of APDs.

Previously reported uses of Si(211) substrates for the growth of compound semiconductors by MBE has only been strictly for group II-VI materials, such as CdTe, ZnTe, and HgCdTe, in which the lattice mismatch is 19.4%, 12.3%, and

19.1%, respectively. Through various X-ray characterization techniques, the presence of microtwins is confirmed, including XRD θ-2θ scans (Rao, Shintri, & Bhat, 2009), and double crystal XRD rocking curve peak widths (Dhar *et al*., 1996). It can be elucidated from the investigation of Te-surface coverage on Si(211) with in-situ X-ray Photoelectron Spectroscopy by Brill *et al*. (2003) that the intrinsic step density of the Si(211) surface is increased many-folds as compared to Si(001). Therefore the number of step-edge nucleation sites is hence increased, while the adatom diffusion is expected to decrease. In addition, previous reports show that the resulting epilayer has an orientation that does not correspond to the Si(211) substrate orientation (Brill, Chen, Dhar, & Singh, 2003; Dhar, Zandian, Pasko, Arias, & Dinan, 1997; Wang *et al*., 2011; Zhao, Jacobs, Jaime-Vasquez, Bubulac, & Smith, 2011). In order words, there exists a rotation between the epilayer and the substrate about the substrate normal as determined by selected area electron diffraction patterns from TEM and XRD measurements. The measured rotation is 3.5° for CdTe/Si(211) (Zhao *et al*., 2011) and 2.66° for ZnTe/Si(211) (Wang *et al*., 2011).

2.5 Summary

In summary, the work that has been done on GaSb/Si heteroepitaxy systems from a structural characterization and growth optimization standpoint, as well as the literature related to the work presented in this thesis is as follows. Despite the introduction of AlSb as a buffer layer, which is effective in attaining a layer-by-layer growth front and a smaller degree of misorientation, the GaSb

epilayer grown thereafter still remains susceptible to a high density of extended defects. The literature has shown that, through the use of various TEM characterization techniques, new understanding of the nature of some defects can be gained. TEM has provided evidence of interfacial misfit dislocations, threading dislocations, and to some extent microtwins. However, comprehension of the crystallographic characteristics of the microtwins, as well as unambiguous and confirmed observation of anti-phase disorder still needs more thorough investigation. Therefore significant attention in our review was placed upon understanding the detection and confirmation techniques of APBs, as well as the effects of their use on a in zinc-blende compound with unusually large Z difference (in the group III and V atoms). Lastly, a possible solution for the suppression of anti-phase disorder in such polar on non-polar systems, previously suggested for group II-VI compounds, was also discussed.

3. Experimental Methods

3.1 Molecular Beam Epitaxy Growth

Group III-V compound semiconductor epilayers (GaSb, GaAs) were deposited on nominal (001)-oriented (±0.5°), vicinal (001)-oriented (offcut 4.7° [±0.25°] towards [110] tilt direction), and (211)-oriented Si substrates using a SVT Associates molecular beam epitaxy (MBE) system. As-received epi-ready wafers were cleaned for 1 min in a 4% HF in deionized (DI) water dip followed by a 30 sec DI rinse immediately prior to their insertion into the MBE load-lock. Before film deposition, both the nominal and vicinal Si(001) substrates underwent a 15 min degassing procedure at 350 °C followed by a thermal treatment at 800 °C for up to 5 min, in order to reconstruct the Si surface into single domain terraces (Neergaard Waltenburg & Yates, 1995; Pehlke & Tersoff, 1991; Sakamoto & Hashiguchi, 1986; Schroder-Bergen & Ranke, 1991). A small number of single steps are expected to remain on vicinal substrates, and a higher number on nominal substrates because of the larger terrace length. GaSb samples are grown at 600 °C at a growth rate of 1 μm/hr with a beam equivalent pressure ratio (V/III ratio) of ~1.2, in the presence of a 5 nm AlSb buffer layer as prescribed by Akahane *et al*. (2004), at a growth rate of 0.1 monolayer/s. GaAs samples were grown at 520 °C at a growth rate of 1 μm/hr with a beam equivalent pressure ratio (V/III ratio) of ~1.5. These growth temperatures have been optimized from preliminary studies at various growth temperatures, yielding the

lowest rocking curves full-width half-maximum for the (004) reflection using double crystal X-ray diffraction, and good overall defect structure through conventional transmission electron microscopy (TEM).

3.2 Transmission Electron Microscopy

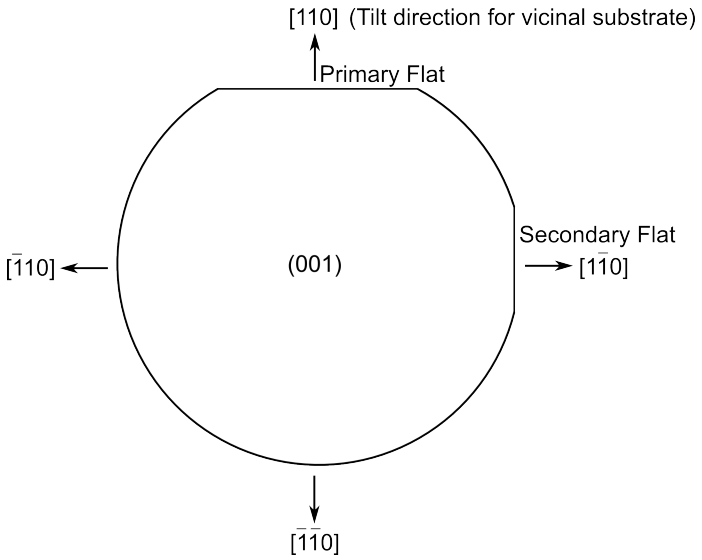

Figure 3.1: Schematic of (001)-oriented Si wafer with its primary and secondary flat orientations labeled.

Epitaxial layers have been characterized in two orthogonal cross-sections with respect to the primary and secondary flats of the Si wafer, namely two {110} cross-sections for the (001)-oriented and a {110} and a {111} for the (211)-oriented specimen. This is so that in the vicinal Si(001), one cross-section is parallel to the [110] miscut direction and the other is perpendicular to it, as shown in Figure 3.1. The specimens were prepared by the standard procedure of mechanical polishing, dimpling, and ion-milling (Gatan PIPS system with 4 keV Ar^+ ions at an incident angle of ±4º) until perforation for electron transparency.

Characterization was carried out with a Philips CM12 conventional transmission electron microscope operated at 120 kV and equipped with a LaB_6 filament.

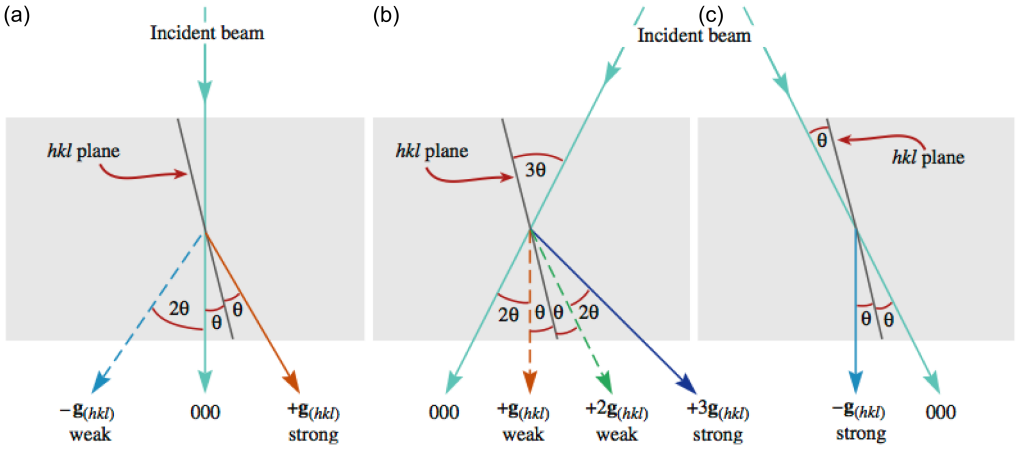

Figure 3.2: Standard two-beam conditions for (a) bright-field with the objective aperture on axis, (b) weak-beam, (c) strong-beam centred dark-field with the objective aperture on optic axis (Williams & Carter, 2009).

Diffraction contrast imaging techniques, including two-beam condition bright-field (BF), strong-beam centred dark-field (DF), weak-beam dark-field (WBDF) and selective dark-field, were used to obtain crystallographic information of the epilayers, as well as study their defect structures. A schematic indicating the setup of the first three standard two-beam diffraction conditions are shown in Figure 3.2. Another interpretation can be considered from the Ewald sphere construction identifying the position of the Kikuchi lines, such as that of BF in Figure 3.3(a, b) and WBDF in Figure 3.3(c, d) denoted as g(3g) conditions. In addition, electron diffraction analysis was performed using selected area electron diffraction (SAED), and convergent beam electron diffraction (CBED) techniques as described by Taftø and Spence (1982).

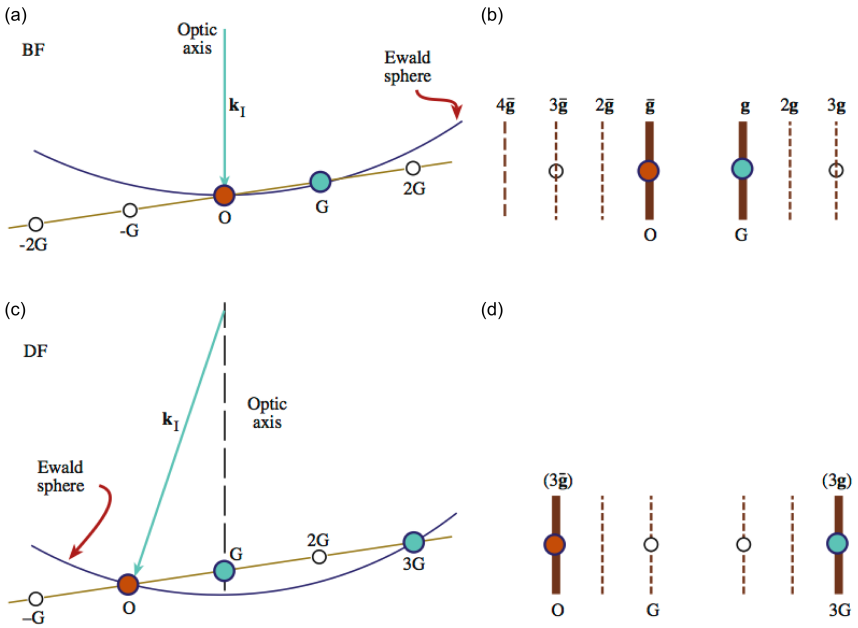

Figure 3.3: The relationship between the orientation of the Ewald sphere and the positions of the Kikuchi lines for (a, b) BF 0(g), and (c, d) WBDF g(3g) diffraction conditions. The two pairs of diagrams are related by tilting the beam, while the specimen is not tilted so that the positions of the Kikuchi lines remain unchanged (Williams & Carter, 2009).

3.2.1 Convergent Beam Electron Diffraction

To confirm anti-phase order in adjacent domains as separated by anti-phase boundaries (APBs), the reversal in crystal polarity (or bond directionality) in these adjacent domains can be confirmed by the CBED technique by Taftø and Spence (1982). Using this technique across APBs, the same set of dynamically scattered high-order Laue zone (HOLZ) lines is opposite in contrast when they cross the same superlattice disc, which demonstrates a reversal in polarity across the boundary. This is due to a π-phase change in the high-order contribution, which are then constructively or destructively interfered (Neave, Larsen, Joyce, Gowers, & van der Veen, 1983; Posthill, Tam, Das, Humphreys, & Parikh, 1988).

Further details of this technique are described in the Literature review section (Ch. 2.3.1).

The CBED analysis was done with the Philips CM12 conventional TEM, with a cryo-stage specimen holder operated at near liquid nitrogen temperature. This holder and temperature were used in order to minimize the thermal diffuse scattering effects in the specimen to enhance the clarity of the HOLZ lines studied, which is especially important when probing domains in a thin film such as these heterostructures.

3.3 Two-Dimensional X-ray Diffraction

Stereographic {111} pole figures were generated using two-dimensional X-ray diffraction (2DXRD) techniques. A Bruker SMART 6000 CCD detector on a Bruker 3-circle D8 goniometer (Bruker AXS Inc., Madison, WI) with a Rigaku RU-200 rotating anode X-ray generator (Rigaku MSc, The Woodlands, TX) and parallel-focusing monochromator optics was used for the data collection. Scans were taken with the detector centred on the {111} 2θ of the material of interest and rotated through 360° of φ in 0.5° increments about the surface normal of the sample similar to the set up in Figure 3.4.

The pole figures are a stereographic projection of the {111} X-ray reflections of all orientations of the crystallographic planes with that particular spacing. The pole figures are oriented with respect to the frame of reference of the Si substrate, such that the top of the pole figures are aligned with the [110] and $[0\bar{1}1]$ direction of the (001)- and (211)-oriented substrate, respectively. Pole

figures are generated by preparing a 1D integration of all frames to determine the combined width of the {111} peaks in MAX3D software (McMaster University) (Britten & Guan, 2007). The peak width was then used to integrate {111} reflections from all frames, including a background and absorption correction for the corresponding material with GADDS (Bruker-AXS) software, resulting in a pole figure. Pole intensities were obtained from pole figures using a circular integration cursor with a 10 pixel radius which was centred on the pole so as to maximize the total intensity captured. All pole intensities were corrected for structure factor and frame exposure times.

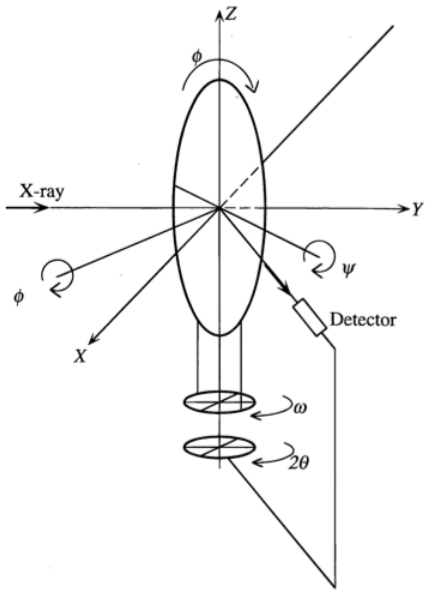

Figure 3.4: Different axial movements used for generating pole figures with 2DXRD (Balakrishnan *et al*., 1997).

4. Results

4.1 Absence of AlSb Buffer Layer

In the absence of an AlSb buffer layer, the GaSb thin film grown at the same optimized temperature of 600 °C has distinct island-nucleated growth morphology. At a thickness of 500 nm, the GaSb had not achieved a layer-by-layer growth front, instead remained as coalesced island upwards of 1 μm in diameter as shown in Figure 4.1(a). These islands, however, are not individually perfect single crystals.

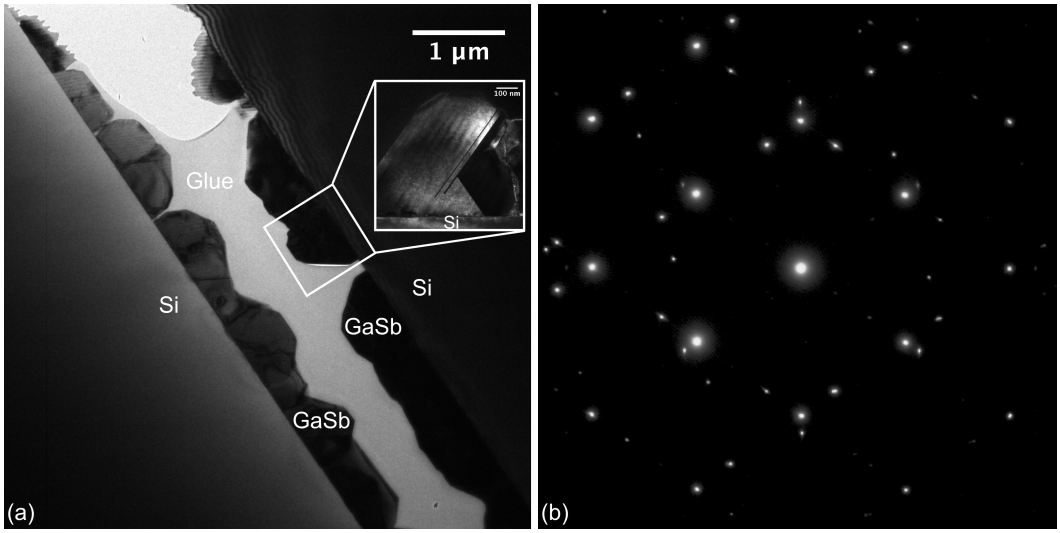

Figure 4.1: 500 nm GaSb epilayer grown on Si(001). (a) TEM [110] zone axis BF image of both $[1\bar{1}0]$ and [110] cross-sections, bottom left and upper right of the image, respectively. (b) [110] zone axis SAED pattern of the particular island shown in the inset of (a), demonstrating extra reflections that arise from twinning.

The SAED pattern (Figure 4.1(b)) of the particular island shown in the inset of Figure 4.1(a), indicates many extra reflections that arise from first-order and second-order twinning. In addition, an array of misfit dislocations exist at the

GaSb/Si interface, as well as some surface roughness into the Si substrate where the interface is observably not smooth. Further analysis has determined that GaSb has taken up presence in these surface pits.

Using selective dark-field diffraction contrast formed with a twin reflection, the twin variants that give rise to the reflection can be identified in real-space in strong contrast. This is important in identifying the boundaries that separate these variants, to better understand the coherency of these boundaries. We have used this technique to demonstrate on the crystallography of an island with a peculiar pentagonal arrangement of four boundaries as shown in Figure 4.2. These boundaries are visible in the bright-field image of the $[1\bar{1}0]$ zone-axis in Figure 4.2(a). The epitaxial variant (Figure 4.2(b)) is isolated using dark-field diffraction contrast formed with a reflection that is exclusive to, and not shared as part of a twinned diffraction pattern. Two first-order twin variants with $(\bar{1}\,\bar{1}\,1)$ and (111) habit planes are identified in Figure 4.2(c) and Figure 4.2(d), respectively. Additionally, two second-order twin variants of the first-order twins from Figure 4.2(c) and (d) are also identified, as shown in Figure 4.2(e) and (f), respectively. All multi-twinned variants are identified using dark-field images that isolate their corresponding twin reflections, which are exclusive to that particular variant and not shared with a higher-order twin. The importance for understanding the nature of these twin boundaries and coexisting variants will be described in the Discussion (Ch. 5).

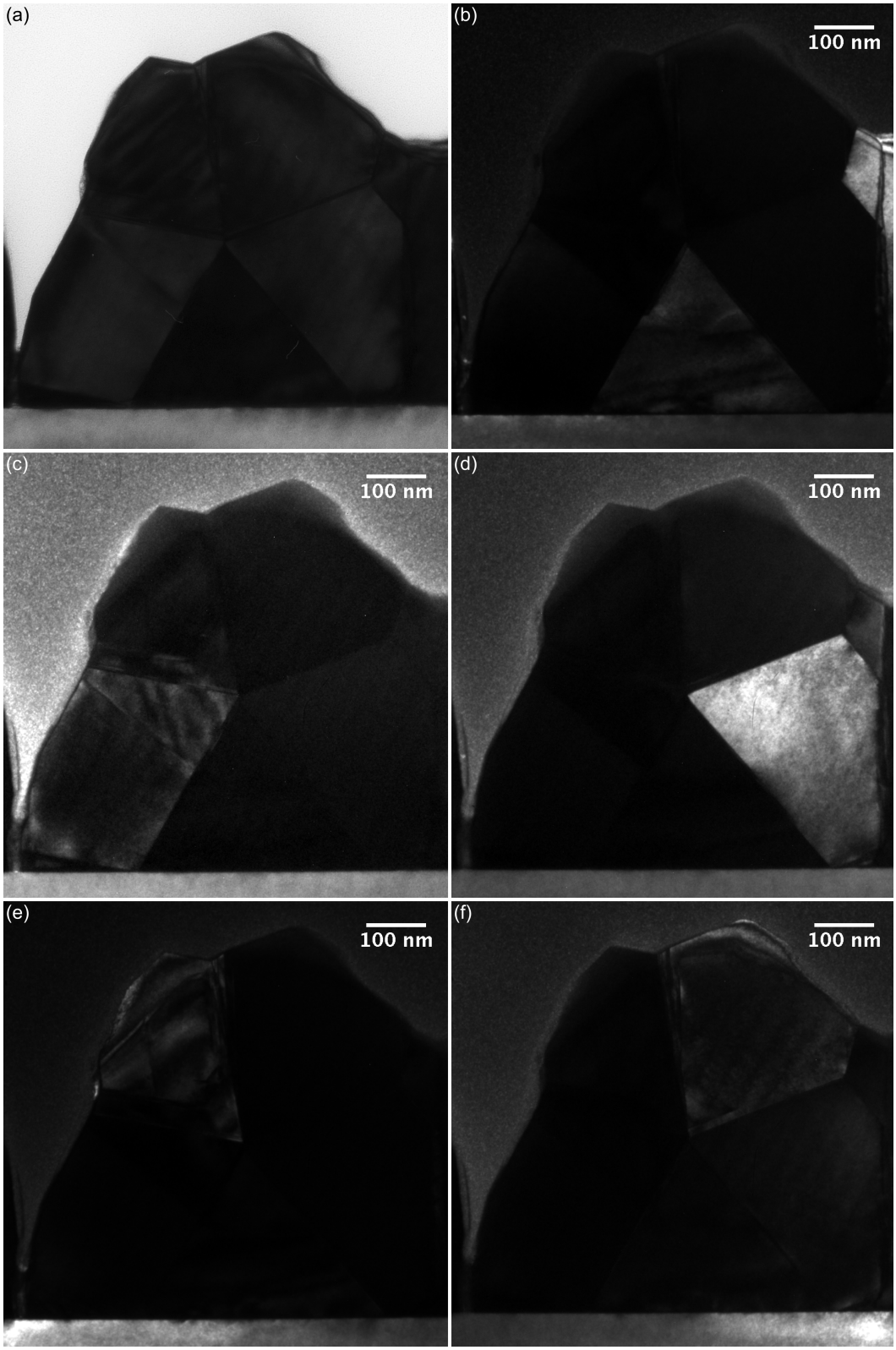
(a)
(b)
100 nm
(c)
100 nm
(d)
100 nm
(e)
100 nm
(f)
100 nm

Figure 4.2: TEM images of the same area of GaSb grown on Si(001), featuring multi-twinning. (a) BF image of the $[1\bar{1}0]$ zone-axis, (b) selective DF formed with epitaxial orientation reflection, (c) selective DF formed with first-order twin reflection, (d) selective DF formed with first-order twin reflection, (e) selective DF formed with second-order twin reflection, (f) selective DF formed with second-order twin reflection.

4.2 Introduction of a Strained-Layer Superlattice

Strained-layer superlattices (SLS) are often introduced in epitaxial films to reduce the propagation of defects during growth. The layer structure schematic of the GaSb epilayer grown on nominal Si(001) in the presence of 5 nm AlSb buffer layer is given in Figure 4.3. A SLS made up of 25 periods of 10 nm AlSb/10 nm GaSb alternating layers, was thus introduced as additional strain field to reduce the threading dislocation density by bending them away from the film surface.

Active GaSb Layer	200 nm GaSb (Te) - 10^{18} cm^{-3}
	400 nm GaSb (Te) - $1x10^{17}$ cm^{-3}
	400 nm GaSb (Be) - $5x10^{16}$ cm^{-3}
SLS – x 25	10 nm GaSb (Be) - $1x10^{18}$ cm^{-3}
	10 nm AlSb (Be) - $1x10^{18}$ cm^{-3}
GaSb Layer	1 µm GaSb (Be) -$1x10^{18}$ cm^{-3}
AlSb Buffer layer	5 nm AlSb (Be) -$1x10^{18}$ cm^{-3}
Substrate	p-Si(001) flat

Figure 4.3: Schematic of epilayer structure with a strained-layer superlattice. The doping concentrations achieve a p-n junction in the active GaSb layer.

4.2.1 Linear Defects

A typical {110} view of GaSb epilayer on nominal Si(001) substrate grown with a SLS as observed through cross-sectional conventional TEM (XTEM) is as shown in Figure 4.4. The micrograph shows a high density of threading dislocations, interfacial misfit dislocations, and microtwins that

propagate to the film surface. A majority of the threading dislocations in Figure 4.4(a) are localized in regions close to the GaSb/Si interface, prior to the SLS. Therefore the SLS does appear to be effective in its ability to repulse away some of the propagating threading dislocations. The propagating microtwins however appear to be unaffected by the strain field induced by the SLS, instead the SLS boundaries appear to get distorted from the intersection of a microtwin.

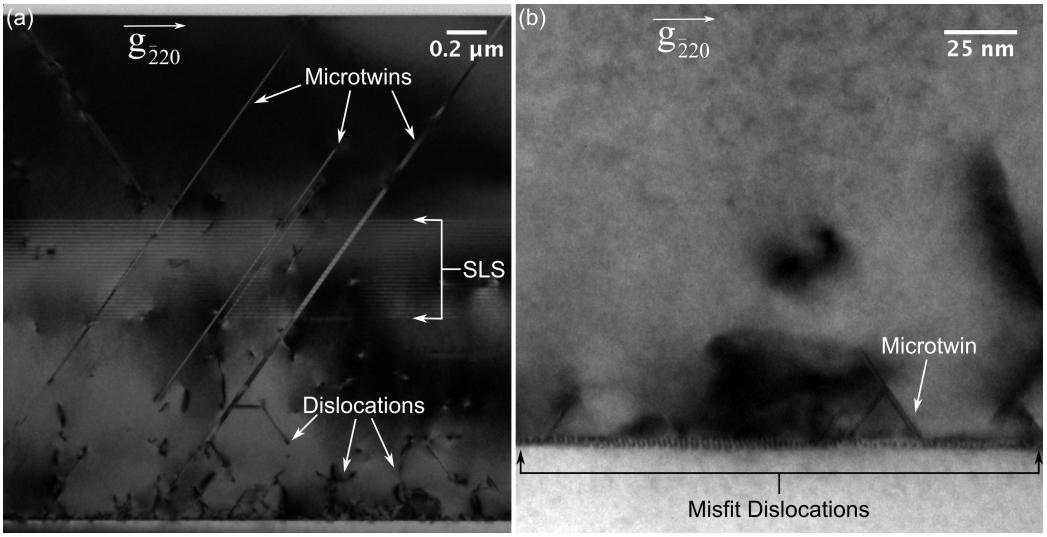

Figure 4.4: TEM two-beam images taken of the (110) view. (a) BF image of the whole epilayer with g = $\bar{2}20$, (b) BF image of the GaSb/Si interface with g = $\bar{2}20$.

A closer look at the GaSb/Si interface in Figure 4.4(b) shows a periodic array of misfit dislocations (MDs) with a spacing of ~ 3.5 nm. It has been reported that MDs in this highly lattice-mismatched heterostructure system are almost exclusively of the pure edge (90°) Lomer type, with Burger's vector along the interface, b = a/2 <110> (Kim *et al*., 2007). Because of this, they are twice as effective at strain relaxation than the 60° type interfacial MDs, and are expected to less likely induce threading dislocations that are detrimental to the

heterostructure. The theoretical average spacing of Lomer dislocations can be derived from the formula $L = b/f$ (Manasreh, 1997), where b is the Burgers vector in GaSb (b = 4.31 Å), and f is the lattice mismatch in GaSb/Si (f = 0.1224). The resulting theoretical average spacing of L = 35.22 Å is closely matched to the measured spacing of 3.5 nm, indicating that the GaSb epilayer should be fully relaxed as the misfit strain is completely compensated by the periodic array of interfacial MDs. This is also in good agreement to the epilayer lattice parameter as measured from double-crystal X-ray diffraction, which was close to the bulk value for GaSb indicating the close to complete strain relaxation.

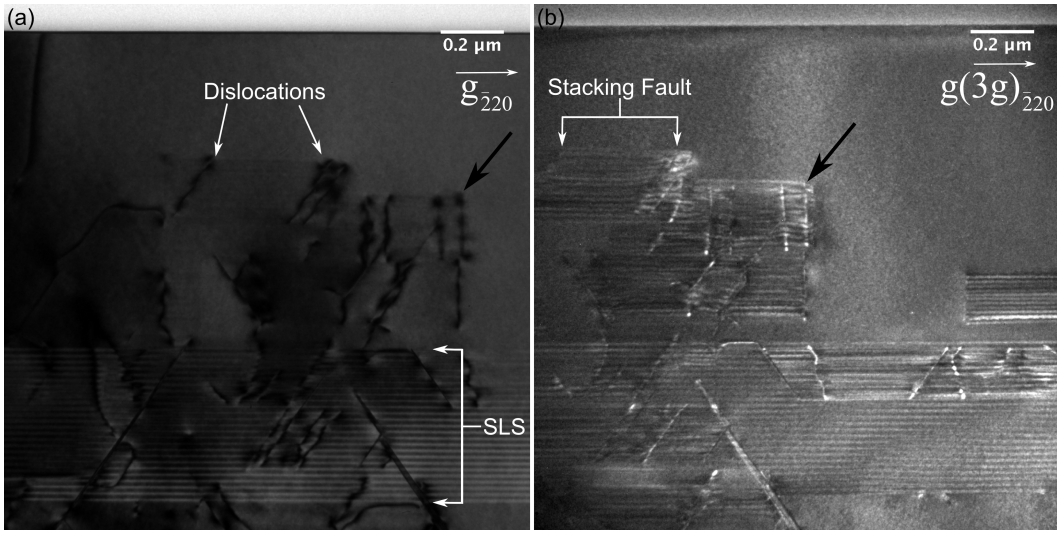

Figure 4.5: TEM two-beam images of the same area featuring stacking faults and their bounding dislocations on nominal Si(001). (a) BF image with g = $\bar{2}20$, (b) WBDF image with g(3g) = $\bar{2}20$. The black arrow shows the area in common between (a) and (b).

With the use of WBDF diffraction condition, other than isolating the cores of the threading dislocations, the fringe contrast of stacking faults can also be made visible. The bright-field image of an area shows threading dislocations as dark line features (Figure 4.5(a)), and there are no additional features between

pairs of dislocations; while the WBDF image in Figure 4.5(b) formed with the complementary reflection of the same area shows the threading dislocations as narrower, bright features. More importantly, there is now fringe contrast between pairs of dislocations in the WBDF image of Figure 4.5(b), which is characteristic of stacking faults. These stacking faults are deduced to lie on the two {111} planes that are not edge-on in this particular cross-section.

4.2.2 Influence on the Growth Front

The insertion of a SLS of alternating layers of GaSb and AlSb allows for the clear visualization of the effect of microtwins on the growth of the films with strong contrast enhanced using the two-beam imaging condition. From the diffraction contrast image, it is possible to identify the tilting of the SLS within the microtwin (Figure 2.9), which is indicative of a change in growth front within said microtwin. The image in Figure 2.9 also shows that the microtwins do not necessarily appear to form right at the interface with the substrate, which is due to the finite thickness of the specimen foils. However, this effect does not take into consideration the propagation of the microtwins in the third dimension in the direction of the electron beam.

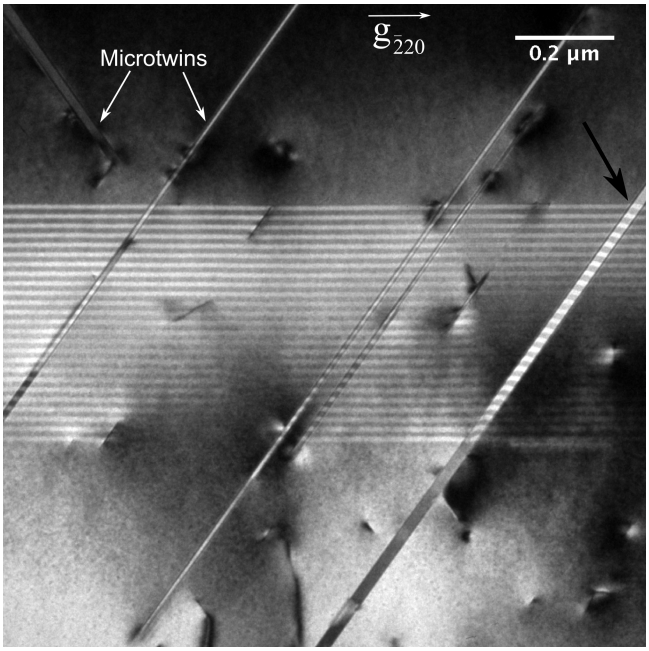

Figure 4.6: Conventional TEM DF image of the AlSb/GaSb strained-layer-superlattice and various microtwins intersecting the layers using the g = $\bar{2}20$ fundamental reflection. Pointed by the black arrow is evidence of a growth front change from planar to stepped due to the microtwin.

4.2.3 Anti-Phase Domains

APBs that originate from the interface and propagate through the film thickness are observed in the following images (Figure 4.7(a), (c), (d)) of GaSb on Si(001) using two-beam condition dark-field imaging with superlattice reflections in XTEM in the [110] direction. A higher magnification view of the same ribbon-like APB (with g = 002) is shown in Figure 4.7(c). As compared to the image formed with the opposite superlattice reflection (g =$00\bar{2}$) in Figure 4.7(d), its fringe contrast is reversed. The bright-field image formed with a fundamental reflection (Figure 4.7(b)) also demonstrates that the invisibility criterion holds true.

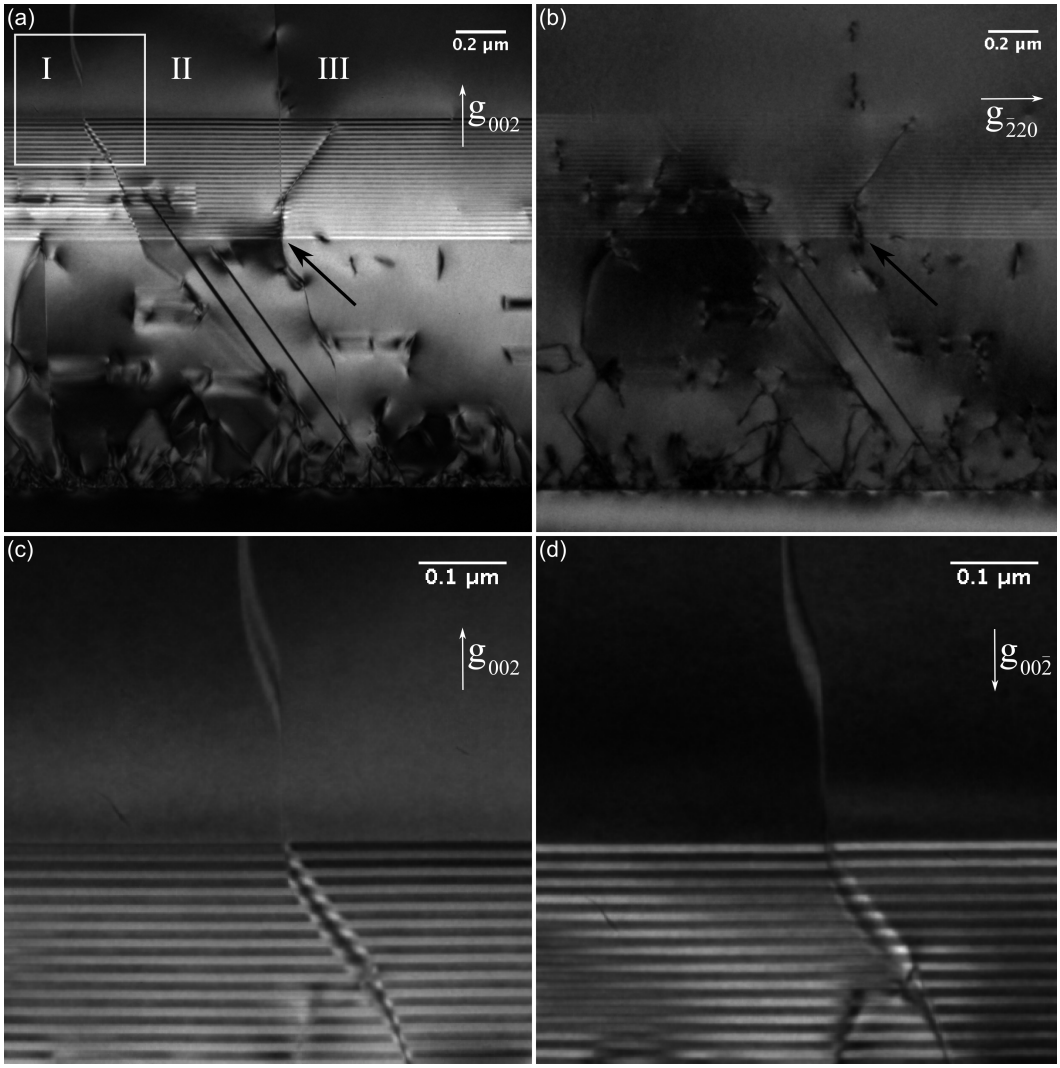

Figure 4.7: TEM two-beam images of the same area featuring APBs on nominal Si(001). (a) DF image with superlattice reflection g = 002, (b) BF image with fundamental reflection g = $\bar{2}20$, (c) detailed view of boxed area in (a), (d) DF image of the same area as (c) with superlattice reflection g = $00\bar{2}$. The black arrow shows the area in common between (a) and (b).

To further confirm that the two planar defects of interest in Figure 4.7(a) are indeed APBs and not threading dislocations, the CBED techniques as proposed by Taftø and Spence (1982) was performed to test if a reversal in crystal polarity was present between the different regions segmented by the boundaries (labeled I, II, III), shown in Figure 4.8. Indeed, the results show that the HOLZ

lines crossing the 002 disc in region II (Figure 4.8(b)) are of the same contrast as those in the $00\bar{2}$ disc in region III (Figure 4.8(f)) and region I (Figure 4.8(d)). The opposite contrast is observed in the complementary discs (Figure 4.8(e), (c), (a) to regions II, III, and I, respectively).

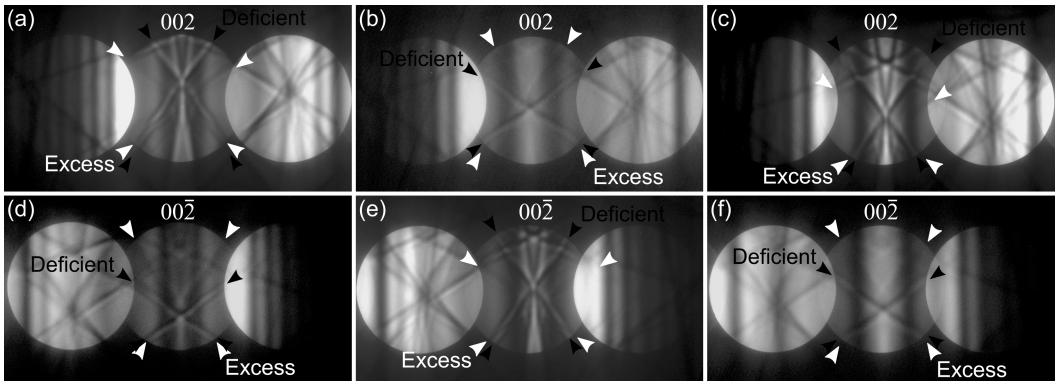

Figure 4.8: CBED pattern of 002 (a, b, c) and $00\bar{2}$ (d, e, f) diffraction discs from regions I (a, d), II (b, e), III (c, f) from Figure 4.7(a), depicting reversal of polarity in region II with respect to regions I and III.

Examples of APBs that are self-annihilated at the Si interface have also been observed for epilayers grown on nominal Si(001) (Figure 4.9). The typical spacing of APBs from one end of the closed-loop to the other for nominal Si(001) substrates is 200 – 500 nm. The majority of the APBs observed in GaSb epilayers grown on nominal substrate under these conditions are those that propagate through the whole film thickness.

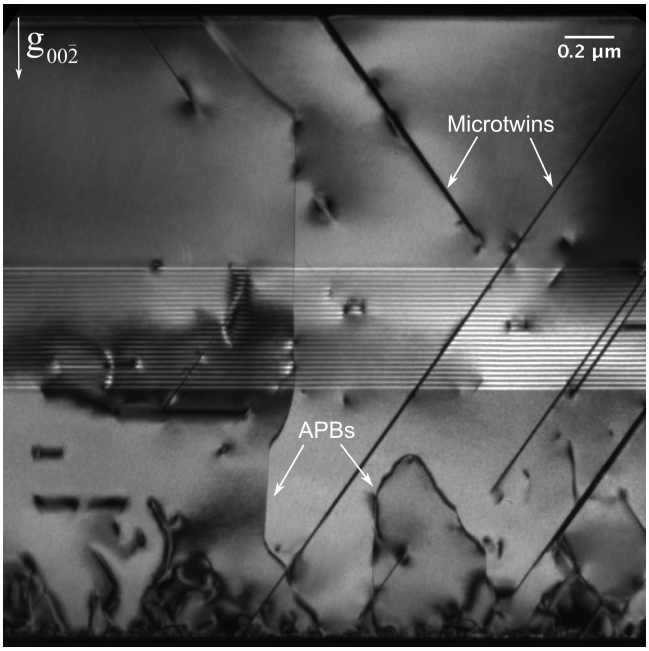

Figure 4.9: DF image of GaSb film on nominal substrate with superlattice reflection g = $00\bar{2}$, showing both propagating and self-annihilated APBs.

4.3 The Role of Surface Steps on Vicinal Substrates

4.3.1 Reciprocal Space Mapping: Two-Dimensional X-ray Diffraction

Figure 4.10 shows the {111} pole figures generated from 2DXRD data of GaAs and GaSb epilayers grown on nominal and vicinal Si(001). The pole figures presented are a stereographic projection of the {111} X-ray reflections of all orientations of the material of interest, oriented with the top of the figure corresponding to the [110] direction of the substrate. The pole positions indicate that the two III-V materials (GaAs and GaSb) have the same symmetry and have variations of one orientation relationship with the Si substrate. The pole figures also indicate a dominant bulk epitaxial phase with a [001]-normal, as well as four additional weaker orientations associated with twins having (111), $(1\,\bar{1}\,1)$, $(\bar{1}\,\bar{1}\,1)$

and $(\bar{1}11)$ habit planes. Two other cubic III-V material systems, InP and AlSb, in conjunction to GaAs and GaSb presented here, are further discussed in Devenyi *et al*. (2011). The major distinction is the evidence of second-order twinning in InP and AlSb samples, which give rise to extra reflections in their respective pole figures. There is also a higher amount of twinning overall in InP and AlSb in comparison to GaAs and GaSb.

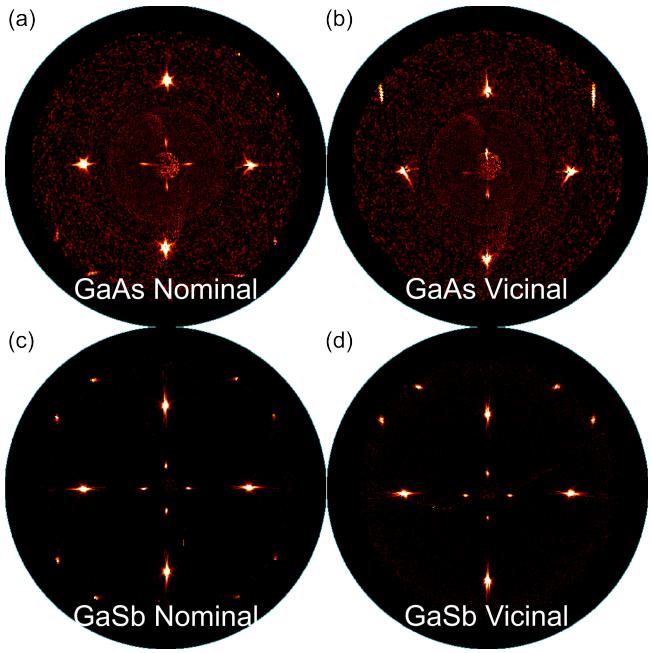

Figure 4.10: Stereographic {111} pole figures of (a) GaAs nominal, (b) GaAs vicinal, (c) GaSb nominal, (d) GaSb vicinal, as generated from 2DXRD. They show a bulk (001) phase plus four twinned variants as identified in Figure 4.11(a). Twin variant intensity is asymmetric for vicinal substrates.

A simulated pole figure, where the origin of each pole is labeled, is given in Figure 4.11(a). These results indicate that all the poles observed from these epilayers are a result of twinning. The experimental pole figures differ from the simulation due to instrumental broadening of poles. The outermost poles are partially visible in the experimental pole figures due to limitations of the

measurement range of samples in reflection, combined with substrate tilt tolerance. The background of Figure 4.10(a) and (b) is higher due to the relatively weaker XRD scattering from GaAs. For films grown on vicinal substrates (Figure 4.10(b), (d)) the centre of symmetry of the pole figure is shifted away from the tilt direction, i.e. towards the step edge.

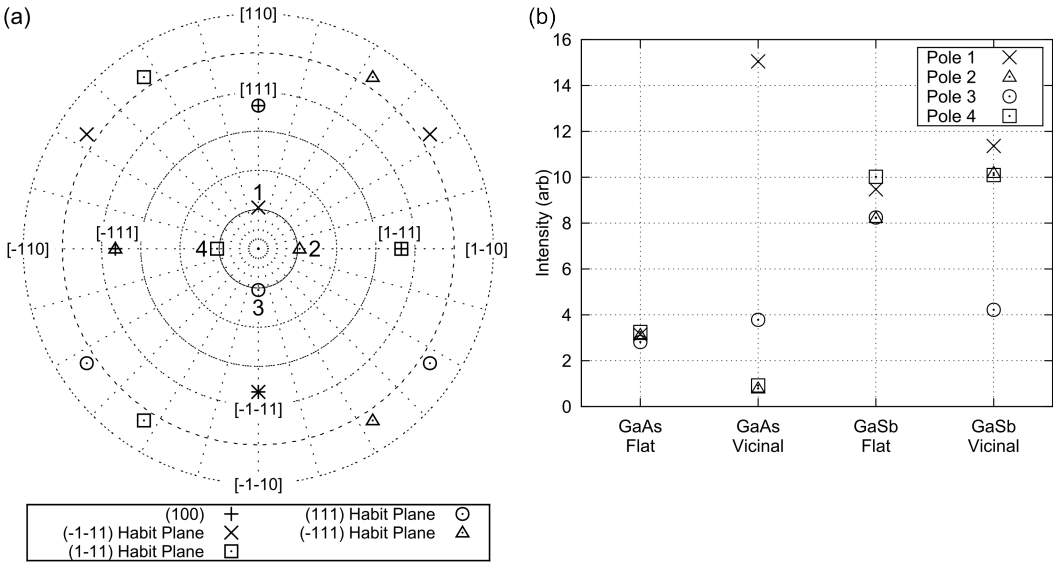

Figure 4.11: (a) Simulated {111} pole figure for a cubic III-V semiconductor film deposited on nominal Si substrate. The pole figure contains poles from the dominant [001] film orientation film and four primary twins along their associated habit plane. The poles associated with each orientation are labeled with unique markers for use in the intensity measurements, and labels on the edge of the pole figure indicate absolute crystal directions of the Si substrate. All reflections from Figure 4.10 are accounted for. (b) Corrected intensity plots of the four orientations marked in (a), via structure factor and exposure time for GaAs and GaSb.

Figure 4.11(b) shows the corrected measured intensity of the unique twin poles, as labeled in Figure 4.11(a). On nominal substrates, pole intensities are equal within experimental uncertainty and hence the twin volume fraction is equal for all four <111> twin plane directions. Important to note is that for films grown

on vicinal substrates, is a 50-75% reduction in the volume fraction of the twin forming opposite to the step direction of the (111) habit plane (Pole 3).

4.3.1 Real-Space Imaging: Conventional TEM

Conventional cross-sectional TEM measurements indicate that microtwins are visible for both the GaAs and GaSb material systems. Selected area electron diffraction (SAED) patterns of areas containing microtwins give rise to additional twin reflections in the form of streaks or spots in positions mirrored across the twin plane direction. Analysis of the SAED patterns indicates that the twin variants in the GaAs epilayers are highlighted in strong contrast with dark-field images formed by isolating only the twin reflection of the dominant variant in the diffraction pattern (Figure 4.12(a)) and (Figure 4.12(d)). In comparison to their complementary DF images, where no particular twin variant is highlighted (Figure 4.12(b) and (e) respectively), the preferential twinning direction is clearly present in GaAs grown on vicinal substrates. This is also true for GaSb grown on vicinal substrates, as shown in Figure 4.12(f).

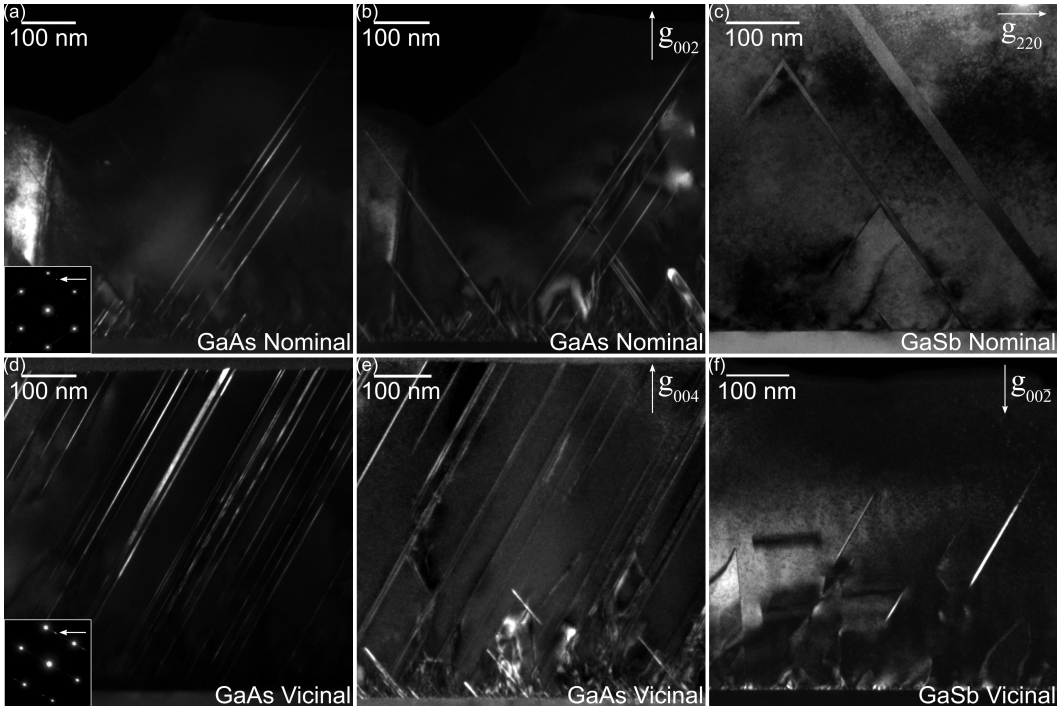

Figure 4.12: TEM images of the $[1\bar{1}0]$ cross-section, a) GaAs Nominal selective DF image of variants with $(\bar{1}\,\bar{1}\,1)$ twin habit plane; b) GaAs Nominal DF image of the same area as a); c) GaSb Nominal BF image; d) GaAs Vicinal DF image of variants with $(\bar{1}\,\bar{1}\,1)$ twin habit plane; e) GaAs Vicinal selective DF image of the same area as d); f) GaSb Vicinal with the preferential twinning direction of $(\bar{1}\,\bar{1}\,1)$ away from step edge (Pole 1), as indicated by microtwins with bright contrast in this DF image; step edge direction is towards the right for all vicinal images.

The asymmetry in twinning directions for vicinal substrates is evident when examining their spatial distribution, as well as propagation into the epilayer with conventional TEM. The preferential twinning direction along $(\bar{1}\,\bar{1}\,1)$ planes away from step edge (Pole 1) induces microtwins that propagate deep into much of the epilayer thickness, as indicated by microtwins with bright contrast in the DF image of GaSb and GaAs shown in Figure 4.12(f) and Figure 4.12(d), respectively. The intrinsic asymmetry to a vicinal substrate becomes very obvious when viewing perpendicular to the tilt direction of [110]. The two edge-on {111}

twin habit planes, namely $(\bar{1}\,\bar{1}\,1)$ and (111) now lie 59.4º (54.7º + offcut angle) and 50º (54.7º – offcut angle) from the interface, respectively. The reduction in peak intensity of Pole 3 from 2DXRD can now be explained by the TEM image of the representative variant, shown in Figure 4.13, which propagates on average ~25 nm from the interface and is small in width as visible in cross-section. In addition, the in-situ RHEED pattern showed a transition from a spotty to a streaky pattern after nearly the same film thickness had been grown, indicating a change in surface morphology. Lastly, despite undergoing the same thermal treatment prior to growth, the observed number of APBs in GaSb is much higher than in the GaAs for both the nominal and vicinal samples.

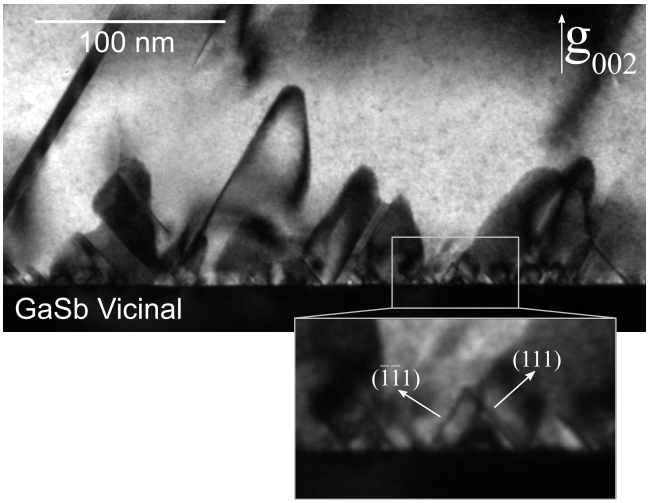

Figure 4.13: TEM DF image of the $[1\bar{1}\,0]$ cross-section of GaSb Vicinal, depicting the nanotwins close to the interface, of the twinning direction of (111) towards the step edges (Pole 3). The black "n"-shaped loops in this DF image formed with a superlattice reflection are APBs. Step edge direction is towards the right of the image.

4.3.2 Surface Steps and Anti-phase Boundaries

APBs in the growth of polar on non-polar semiconductors have been mainly attributed to the presence of single steps at the substrate surface. Because of this, a higher number of APBs is expected to result on a vicinal substrate, which has a higher density of surface steps, and hence steps with shorter terrace lengths. Cross-sections of GaSb epilayers grown on vicinal substrates are examined. There exists an asymmetry in the distribution and propagation of APBs when viewing the cross-section that is under the asymmetry of the offcut from the substrate, as shown in Figure 4.14. The APBs in Figure 4.14 are the black, ribbon-like closed-loops at the interface, which are referred to as self-annihilated APBs. In comparison to the sample grown on nominal Si(001) substrate, the ratio of self-annihilated to propagated APBs increases drastically. Secondly, the typical spacing of self-annihilated APBs from one end of the closed-loop to the other for has decreased to 20 – 50 nm for vicinal Si(001) substrates (as compared to 200 – 500 nm for nominal substrates). Therefore the size of the APDs has decreased drastically for vicinal substrates. It can also be noted that many of these APBs, similar to APBs on nominal substrates, lie on {110} planes edge-on to the incident beam. However, these {110} planes are now affected by the offcut, and are tilted away from the step edge by the offcut angle (i.e. 4.7° in this case).

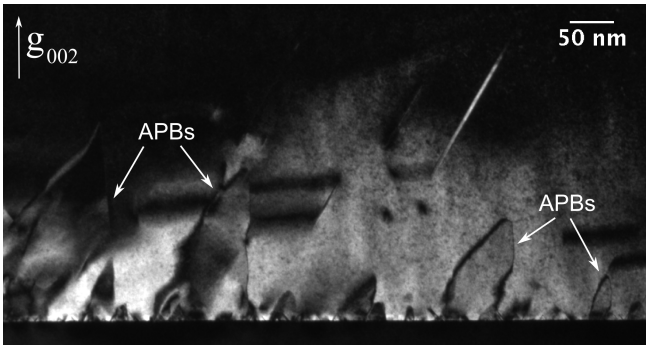

Figure 4.14: TEM superlattice DF image (g = 002) of the $[1\bar{1}0]$ cross-section of GaSb on vicinal Si(001), illustrating the high number of self-annihilated APBs at the interface. Step edge direction is towards the right of the image.

4.4 The Si(211) Alternative

A texture analysis can be applied to thin film samples with two-dimensional X-ray diffraction (2DXRD) by isolating the 2θ for GaSb {111} and generating a pole figure. The GaSb (111) pole figure as shown in Figure 4.15(a) is a stereographic projection of all the orientations present in the GaSb epilayer grown on Si(211). There is clearly more than just the reflections from an epitaxial orientation present in the sample, including first-order twinning about three {111} planes, as well as three sets of reflections from second-order twinning from the first-order twinning direction with the highest intensity of reflections. A simulated pole figure containing all seven orientations generated by twinning operations, as predicted to be present in the sample is shown in Figure 4.15(b), and matches the experimental results remarkably well.

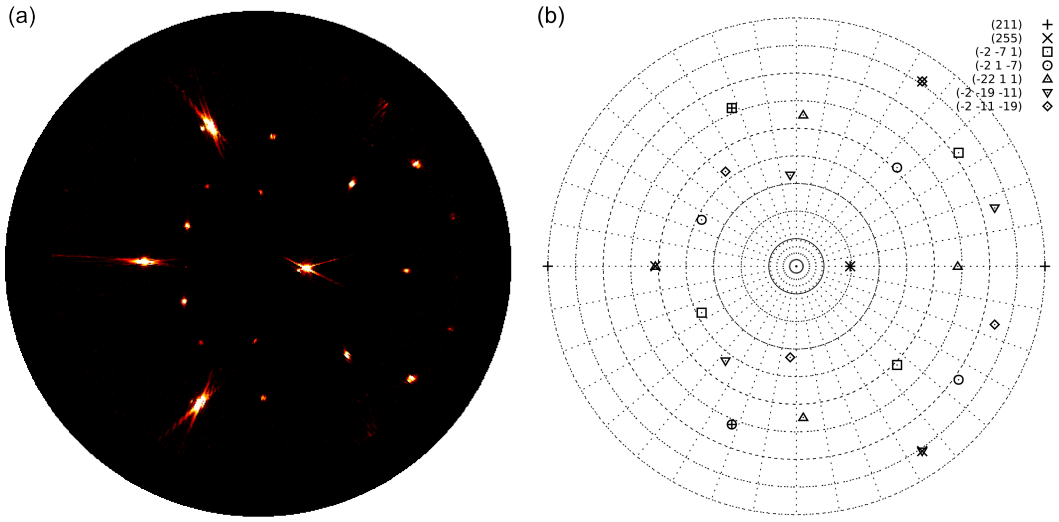

Figure 4.15: Pole figure of GaSb <111> reflections of GaSb epilayer grown on Si(211). (a) experimental, (b) simulated.

Two TEM views in $(0\,\bar{1}\,1)$ and $(1\,\bar{1}\,\bar{1})$ cross-sections of the epilayer grown on Si(211) are as shown in Figure 4.16(a) and (b), respectively. The alternating banded structure in the $[0\,\bar{1}\,1]$ view direction is due to an alternating structure of the epitaxial orientation, and one of first-order twinning with a (111) habit plane. Looking from the perpendicular direction of $[1\,\bar{1}\,\bar{1}]$, these same twins are visible as large bands lying parallel to the interface (Figure 4.16(b)). First-order twinning with a (111) habit plane is the predominant twinning plane in the GaSb on Si(211) by three orders of magnitude based on the pole figure intensities. From a combination of the observation in two perpendicular directions, the twins with (111) habit planes exist in a striated nature with the epitaxial variant when viewed down $[0\,\bar{1}\,1]$, and lying parallel to the interface over a long-range order in the $[1\,\bar{1}\,\bar{1}]$ direction.

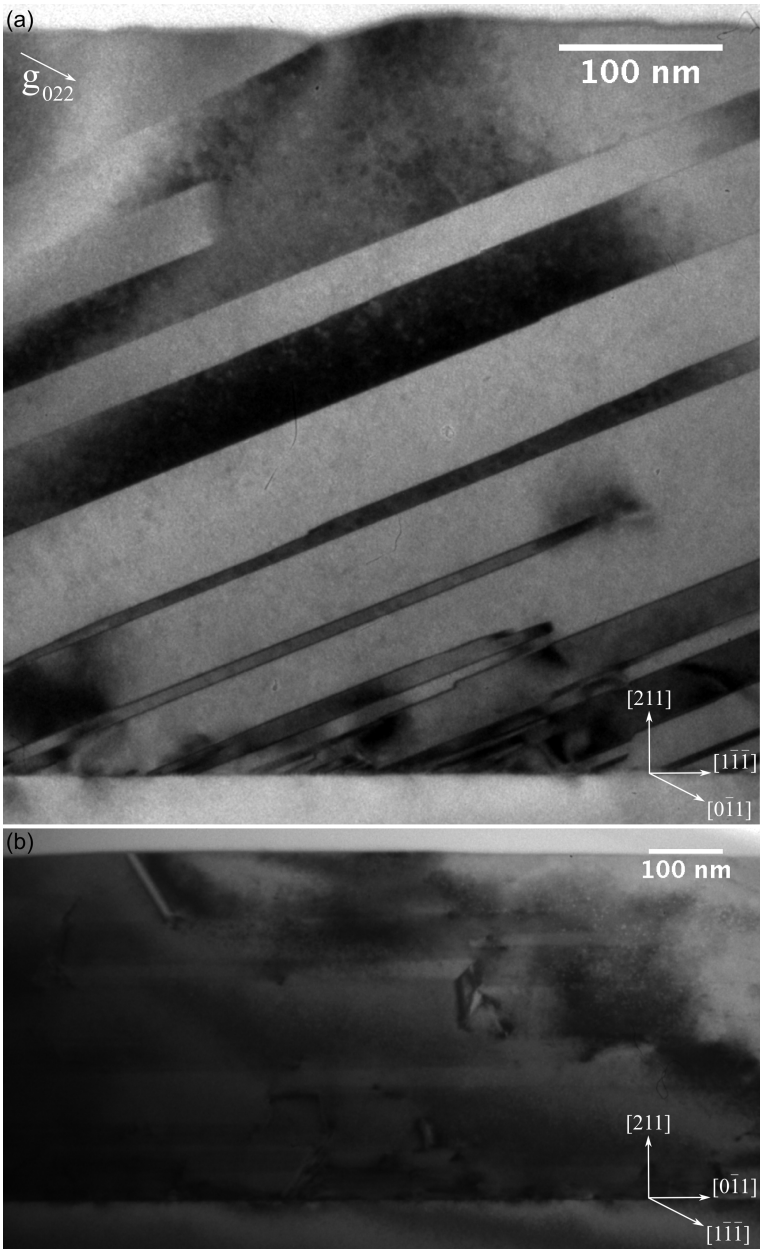

Figure 4.16: (a) Two-beam BF image of the $(0\bar{1}1)$ view with g = 022, (b) BF zone axis image of the $(1\bar{1}\bar{1})$ view.

A SAED pattern from the $[0\bar{1}1]$ zone axis of the area in Figure 4.16(a) is shown in Figure 4.17. The extra reflections are due to the first-order twins about the (111) habit plane. There exists a detectable misorientation between the set of

reflections from the Si substrate and that of the GaSb epilayer (both epitaxial and twinned orientation) of 2.5° towards $[\bar{1}\,1\,1]$ direction.

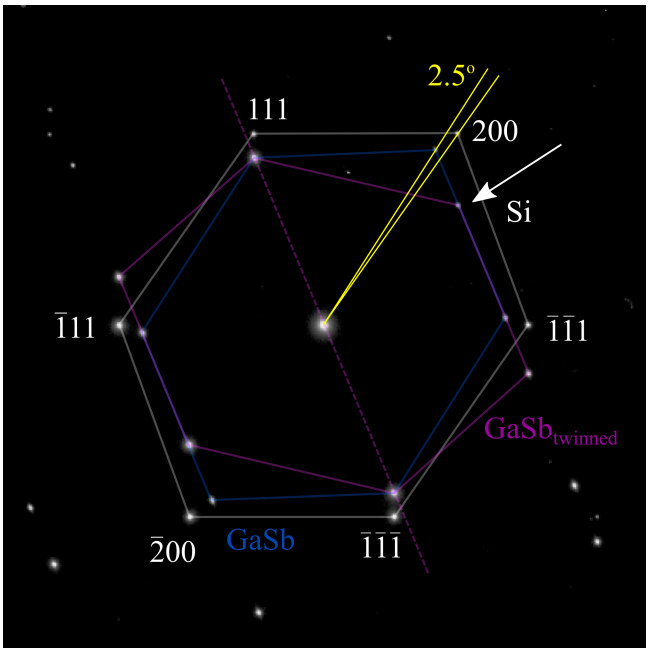

Figure 4.17: Selected area electron diffraction pattern (DP) of the $[0\,\bar{1}\,1]$ zone axis of the area from Figure 4.16(a), showing extra reflections that result from twinning about (111), and a 2.5º rotation between the GaSb and Si DP towards the $[\bar{1}\,1\,1]$. The selective DF image of Figure 4.18(a) is formed using the twin reflection arrowed.

Looking closely at the GaSb/Si interface in the $(0\,\bar{1}\,1)$ cross-section, the alternating regions of epitaxial and twinned orientations can be differentiated from a selective dark-field image (Figure 4.18(a)) formed using one of the twinned reflection spots highlighted in Figure 4.17. The twins with (111) habit planes are in bright contrast in Figure 4.18(a), while the epitaxial regions are in dark contrast. In comparison to the bright-field image with g = 022 of Figure 4.18(b), it is clear that the jagged features at interface (seen in detail in the inset) belong to the epitaxial regions. This is indicative that misfit dislocations are

present at the interface where the epitaxial region meets it, and that it is possible that they are not present where the twinned region meets the substrate.

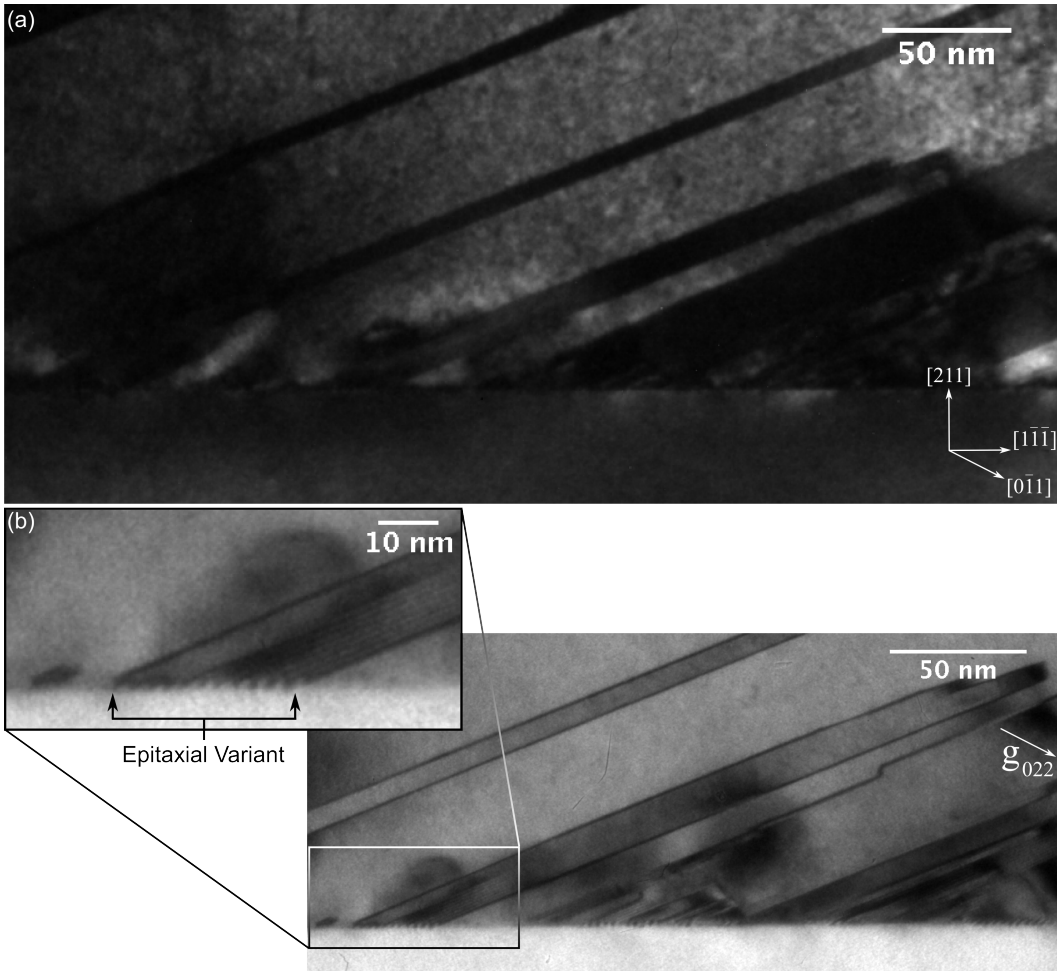

Figure 4.18: TEM images of the $(0\bar{1}1)$ cross-section. (a) Selective DF image formed with a twin reflection so the twinned regions are in bright contrast, (b) BF image with g = 022 with the inset showing the details of the jagged features that are only at the epitaxial portions of the interface.

5. Discussion

In this chapter, we will discuss the experimental results on GaSb/Si heteroepitaxy presented in Ch. 4. Starting with the nature of the unique pentagonal geometry common in multiply-twinned fcc-like crystal structures, observed in our epilayers in the absence of AlSb as a buffer layer. Followed by the likely origin of APBs and their specific similarity and differences in GaSb/Si systems, as compared to the commonly studied GaAs/Si system. Next, the role of vicinal substrates on the suppression of microtwins along one of the four {111} habit planes, and the proposed mechanism for such a phenomena is explained in detail. Also, from the study of microtwins on vicinal substrates, the effects of vicinal substrates on the formation of APBs can be understood. These effects that are characteristic to the GaSb/Si system, can be surmised through the mixed domain nucleation that is anticipated. Lastly, an explanation for the tilted epitaxy observed in growths on (211)-orient Si substrate is elucidated.

5.1 Geometrical Frustrations from Multiple-twinning

When multiple variants of high-order twinning coexist in an area, they commonly arrange in a pentagonal geometry such as that of Figure 4.2. This type of geometry arises from the intersection of five variants, i.e. one epitaxial, two first-order twins, and two second-order twins. A similar geometry has been observed in heteroepitaxy of GaP on Si(001) by high-resolution TEM (Ernst & Pirouz, 1989). Comparable to examples in previously studied fcc multiply

twinned particles or fcc homoepitaxy, if each of the variants is considered as a tetrahedron made up for their {111} faces (Stowell, 1975), the nucleation of such multiple-twinning behaviour in the heterostructure can be easily visualized. Simply said, the two tetrahedra from second-order twinning (OAEF and OADL) do not have their faces match exactly, leaving an empty wedge of OADPE from Figure 5.1(a).

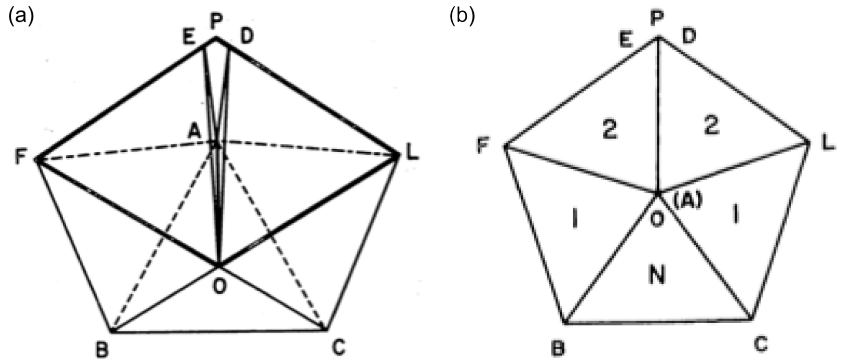

Figure 5.1: Idealized schematics of multiply twinned variants in a pentagonal geometry, (a) a pentagonal geometry made up of five tetrahedra where a wedge (OAEPD) remains from two faces of the neighbouring second-order twin tetrahetra (Ino, 1966), (b) view of (a) along OA showing the pentagonal symmetry and labeled with the order of twinning in each tetrahedron (Ino & Ogawa, 1967).

This is an example of a three-dimensional geometrical frustration, common in tetrahedral packing such as that in fcc and fcc-derived crystal structures. Direct observations of such multiply twinned particles have failed to detect such a void indicating the evidence of an empty wedge (Komoda, 1968). From this, it has been concluded that these gaps have been accommodated by elastic strain of the whole structure to provide higher degree of coherency. This is also a likely explanation in the case of the GaSb epilayer without AlSb as a buffer layer (Figure 4.2), as there exists no empty wedge. Instead there is an interface that is not perfectly edge-on and coherent when viewed down the $[0\,\bar{1}\,1]$ zone axis.

The GaSb/Si system results in a GaSb epilayer that is compressively strained. Therefore it is highly beneficial for the epilayer to relax to its bulk lattice size through the presence of such gaps, which is a likely driving force for such a multi-twinned geometry.

5.2 Anti-Phase Domains

APBs are invisible due to the invisibility criterion ($\mathbf{g}.\boldsymbol{R} = 0$) in bright-field (and dark-field) images formed with fundamental reflections, as shown in the bright-field image of Figure 4.7(b). Isolating the contrast of superlattice reflections is able to detect boundaries in which a relative rigid body translation exists, such as the one intrinsic to APBs along {110} planes, with a vector of $\boldsymbol{R} = a/4 \langle 111 \rangle$. Because both APBs in Figure 4.7(a) are seen edge-on in cross-sectional TEM in this viewing direction, the APBs are expected to lie on or close to the {110} planes perpendicular to the beam direction. Based on the work of Holt (1969), it can be said that MBE growth typically induces growth conditions for stoichiometric composition, therefore it is expected that APBs of the stoichiometric type (ones on {110} and {113} planes) are favoured. This type of APBs is expected to still have electrostatic charges (Holt, 1969), which would be especially detrimental if they were present in the active regions of a device structure. In zinc-blende structure, there are only two ways in which the sublattices can be occupied, therefore hypothetically there can only be two domains of different occupancy scheme in contact with one another (Holt, 1969). This also explains why APBs must either be closed surfaces, such as those that

self-annihilate and coincides with the Si interface, or propagate and emerge at free surfaces (Holt, 1969) such as the two APBs in Figure 4.7(a).

A reversal in polarity would be indicative of the change in bond directionality, equivalent to a $\pi/2$ rotation about the substrate normal, which is the other contributing crystal symmetry operation of an APD. The CBED patterns of opposite superlattice discs, 002 and $00\bar{2}$ from the three regions are as shown in Figure 4.8. It is clear that the HOLZ lines crossing the 002 disc in region II (Figure 4.8(b)) are of the same contrast as those in the $00\bar{2}$ disc in region III (Figure 4.8(f)) and region I (Figure 4.8(d)). The portion of the sample in region I is unfortunately much thicker, therefore it is contributing more to the background of the dynamically scattered HOLZ lines and the $00\bar{2}$ line itself. This can explain the dark background on the HOLZ line pairs in Figure 4.8(d) that are otherwise clearly excess lines in the $00\bar{2}$ disc from region III (Figure 4.8(f)). The remaining CBED patterns of the opposite superlattice reflection (Figure 4.8(a), (e), (c)) show the crossing of HOLZ lines of complementary contrast to their counterparts (Figure 4.8(d), (b), (f), respectively), as expected in a non-centrosymmetric structure such as zinc-blende. For example, the excess HOLZ lines in the $00\bar{2}$ disc of region III (Figure 4.8(f) is deficient in its 002 disc (Figure 4.8(c)). This CBED analysis indicates that region I and III are of the same polarity, and opposite to the polarity of region II. It can be concluded that the two boundaries separating the three regions are indeed APBs.

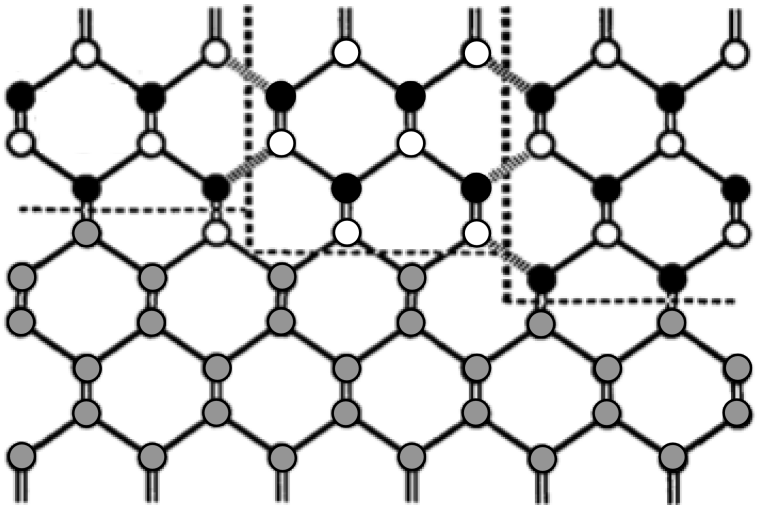

Figure 5.2: Schematic representation of mixed species of first layer atoms at the presence of single steps in the Si substrate, where the formation of APBs is avoided along the {110} planes normal of the substrate surface (dotted lines), adapted from (Georgakilas *et al*., 1993).

The possible origin of APBs as described in an earlier section (Ch. 1.3.3) is the incongruent nucleation of domains of opposite bond directionality at the occurrence of substrate single steps, when assuming that an exclusive element is laid down as the first atomic layer. A secondary case is the possibility of nucleating both Ga-prelayer and Sb-prelayer domains on the same terrace, which would also cause a reversal in bond directionality inducing an APD. As described by Devenyi *et al*. (2011), the low sticking coefficient of Sb-atoms to the Si substrate and the much stronger affinity of Ga-atoms to Si will induce a mixed nucleation of both Ga- and Sb-prelayers at the sample growth temperature presented here. Further details regarding the evidence elucidating the mixed nucleation of GaSb is discussed in a later section (Ch. 5.3.1). This is a majorly differentiating characteristic as compared to epilayers of GaAs grown on Si(001), in which it is possible to induce the nucleation of an exclusive element as reported

by Bringans *et al*. (1991). Therefore both origins of APBs must be taken into account for the GaSb/Si system. Under the assumption that the extent of the Si substrate surface treatment achieved is the same in the GaAs and GaSb samples, then APBs that result from mixed nucleation on the same terrace are much more likely in GaSb. This is in good correlation to the experimental results comparing the two types of epilayers, where the density of APBs is significantly lower in GaAs. In the case that the first atomic layer specie is reversed at a single step, hence reversing the domain, it will actually avoid the formation of an APB at the single step, as in the case in Figure 5.2.

5.3 The Role of Surface Steps on Vicinal Substrates

Island nucleation followed by coalescence (i.e. the Volmer-Weber growth mode) is frequently observed for III-V thin films (Akahane, Yamamoto, Gozu, Ueta, & Ohtani, 2005; Ernst & Pirouz, 1989; Fang *et al*., 1990; Noh *et al*., 2007) and is, in fact, anticipated for the growth parameters used in our film growths. Both substrate strain and interfacial energy play a strong role in determining the size of the initial islands during nucleation. After their initial formation, subsequent island growth occurs on the {111} planes, creating pyramidal structures that grow both laterally and in height. For III-V systems, stacking along the <111> directions consists of alternating layers of group III- and group V-terminated surfaces, where two of the exposed surfaces are $(111)_A$ with Ga triply bonded, and the other two are $(111)_B$ with Sb triply bonded. These two types of surfaces assemble at different rates. Such a growth mode can continue

indefinitely, but often transforms into a layer-by-layer growth once some critical thickness is achieved (Tersoff, van der Gon, & Tromp, 1994).

Epitaxial twins occur when atoms stacked on a {111} plane shift from their designated positions during growth, resulting in a stacking fault, characterized by a 180º rotation in bond directionality about the plane normal. Atoms bonded to the next layer are likely to follow the stacking order defined by their nearest and next-nearest neighbor and continue the stacking sequence set out after the stacking fault, creating a rotation twin of the first region. A subsequent stacking fault will then rotate the next layer back to its original orientation, bounding the twinned region. The stacking fault energy (SFE) for a system is the measure of how costly it is for a single crystal plane to be misordered from its expected stacking sequence.

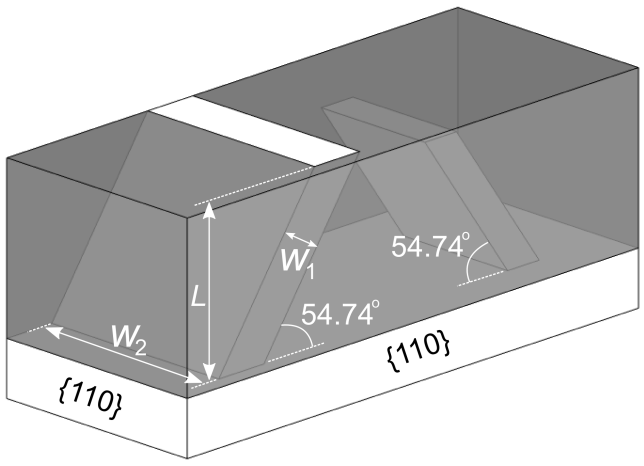

Figure 5.3: Schematic of two twins on a nominal surface, embedded within a film. Twin dimensions with widths (w_1, w_2) and length (L) are labeled.

The total volume (V) of all twins in a film is given by Eq. (5.1) and schematically shown in Figure 5.3:

$$V \cong \sum_{1}^{N} w_1 w_2 L \sin(54.74^\circ) \tag{5.1}$$

The first factor impacting the volume of twins in an epilayer is the number of twins, *N*. This parameter is driven primarily by the SFE, but can also be influenced by the number of nucleation sites. Atomic registration errors on {111} growth planes are expected to occur fairly frequently, as their probability is inversely proportional to the SFE, and SFE is only a fraction of the average thermal energy of an atom during growth (Ernst & Pirouz, 1989). The formation energy of stacking faults is critical to the formation of microtwins, this is to say that when this energy is lower, the probability of a stacking fault, and hence twin formation, increases (Oda, 2007). In the case of GaAs and GaSb, their reduced SFE (the energy per atom in a fault plane) is very similar, with high values of 47 and 53 meV/atom, respectively (Gottschalk, Patzer, & Alexander, 1978). Higher assembly rates on the fault plane can also lock in stacking faults that could otherwise be corrected in order to minimize energetics. The second factor, *L*, is the vertical length that the twins propagate through the epilayer, a value that generally is the full thickness of the epilayer. The last two parameters impacting twin volume are the width in (w_1) and perpendicular to (w_2) the fast-growth direction. The width of the twin in the fastest growth direction is determined by the interplay between the SFE and the assembly rate of that plane. The twin width perpendicular to the fastest growth plane is determined by the size of the island in that dimension, which is influenced both by the chemistry and misfit of the epilayer-substrate interaction.

5.3.1 Comparison of GaAs and GaSb Epilayers

In GaSb films grown on vicinal substrates, there is a 50 – 75% reduction in the volume of twins contributing to Pole 3 (twins with (111) habit plane). This corresponds to a substantial reduction in twin formation opposite to the tilt direction. GaAs, however, is unusual in that it exhibits a strong reduction in twins for directions perpendicular to the step direction (Pole 2 and 4), and an increase in twins towards the tilt direction (Pole 1 >> Pole 3). The TEM studies of Xie *et al*. (1990) on GaAs epilayers grown on vicinal Si substrates observed with conventional TEM correlate well with our observations of As-initiated vicinal GaAs films. Irrespective of the rotation in tilt direction to the perpendicular <110> between Xie's work and the work presented here, the same very low density and equal distribution of microtwins with {111} habit planes perpendicular to the tilt direction (Pole 2 and 4) is evident. Xie's work proposed preferentially oriented island nucleation, and claimed that the asymmetric distribution of microtwinning is due to the two $(111)_B$ planes that are aligned with the offcut exhibiting a faster growth rate.

The reductions in the Pole 2 and 4 twin variants (with $(\bar{1}11)$ and $(1\bar{1}1)$ habit planes, respectively) are not observed for GaSb, or the other III-V systems (i.e. InP and AlSb) as discussed in Devenyi *et al*. (2011), indicating that the fastest-growing plane cannot be solely responsible for such reductions. The single domain nucleation achieved by Xie *et al*. due to Ga and As equal bonding preference to Si (Bringans *et al*., 1988) cannot be guaranteed in other systems due

to the relatively lower bonding affinity of Sb (Kubiak, 1985) and P (Kiyota & Inada, 2001). These other systems instead exhibit a behavior in the distribution of microtwins that is a combination of the As-initiated and Ga-initiated GaAs, as demonstrated by Xie *et al.*, indicating mixed domain nucleation (both group III and V atoms as first atomic layer species). Despite the effort to utilize a group V-soaking prior to growth, the high affinity of group III atoms for Si can easily displace any weakly bonded group V atoms, especially at higher growth temperatures. In growths of group III-initiated nucleation, the fastest growing planes remain as group V planes, but are rotated to the two perpendicular {111} orientations (see GaAs-B from Figure 5.4) not under the influence of the substrate offcut asymmetry, as claimed by Xie *et al*. Therefore, in the event of mixed domain nucleation, the asymmetric preferential growth of microtwins tilted towards the tilt direction in III-Vs grown on vicinal Si cannot be attributed exclusively to the faster growing group V planes.

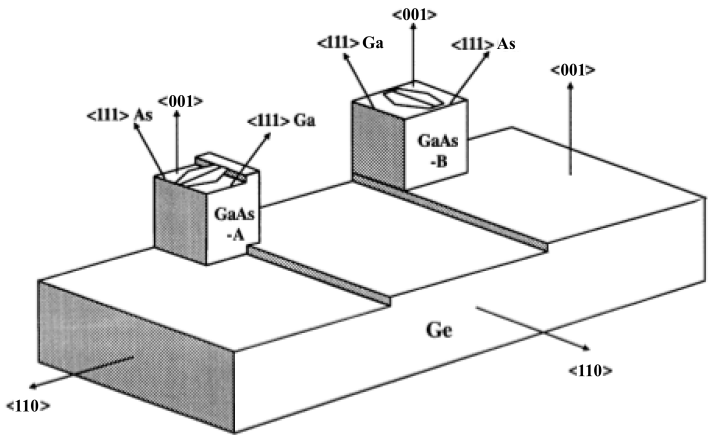

Figure 5.4: The two possible sublattic allocations of Ga and As atoms in GaAs grown on Ge(001) substrate. GaAs-A and GaAs-B represents if the first atomic layer on the Ge surface is As and Ga, repectively (Li, Lazzarini, Giling, & Salviati, 1994).

Previous work by Wei and Aindow (1994) on GaAs epilayers on vicinal Si concludes that under a balanced Ga- and As-initiated flux, it is expected to achieve a layer-by-layer growth mode. They proposed that the high density of twins with habit planes towards the tilt direction, in combination with few twins on all other habit planes, is due to the deformation resulting from the residual misfit associated with the heteroepitaxy. The critical resolved shear stress (i.e. the threshold value of stress necessary to cause atomic planes to slip) as calculated by Wei and Aindow (1994) along the <112> slip direction in the {111} planes towards the tilt direction is over 4% higher than all other slip systems. This means the likelihood of slip in this direction is lower, so deformation twins would more likely form. However, this slip direction is not one of the two contributing partial dislocations (from the dissociation of a perfect dislocation along an interfacial <110>) responsible for the formation of a stacking fault common in such epilayers. In addition, the microtwins observed by Wei and Aindow (1994) do not exhibit a lenticular morphology, as characteristic of deformation twins. Therefore the microtwins observed cannot be exclusively or even primarily be due to deformation, as their asymmetric distribution cannot be explained by the anisotropy in resolved shear stresses alone.

Comparing nominal and vicinal samples, there is an increase in the mean intensity of twins, which can be attributed partially to an increased number of preferential nucleation sites during initial growth, thus increasing the number of twins that can form. Next, there is a drastic enhancement in the fraction of twins

with $(\bar{1}\,\bar{1}\,1)$ habit planes oriented towards the tilt direction in GaAs, which is not observed for GaSb. This phenomenon is evident in both the 2DXRD intensity of Pole 1 (see Figure 4.10(b)) and the DF TEM image (see Figure 4.12(d)). We can surmise from Xie *et al*. that the As-initiated GaAs growth induces an exclusively As-prelayer which leads to a domain in which $(111)_B$ surfaces are on (111) and $(\bar{1}\,\bar{1}\,1)$ aligned with the step direction. The high assembly rates of those planes increase the probability of errors in the form of stacking faults, which in turn, increases the total number of twins nucleated, *N* from Eq. (5.1).

In the case of GaSb with its mixed domain nucleation, the enhancement in the $(\bar{1}\,\bar{1}\,1)$ fast-assembly surface is diluted by the even distribution to the adjacent $(1\,\bar{1}\,1)$ and $(\bar{1}\,1\,1)$ planes of equal assembly rates. Because of this, fewer stacking errors occur in the $(\bar{1}\,\bar{1}\,1)$ and (111) planes, and the number of twins nucleated along those planes are decreased. The effects of this enhancement in the fraction of twins in III-Vs (including GaAs) is expected to be less pronounced with increasing growth temperature, where the group V-prelayer atoms are more likely to desorb, causing mixed nucleation and results that are more comparable to that of GaSb. The presence of single steps on vicinal substrates can also affect this enhancement phenomenon, as they cause a rotation of domains, which result in APBs. The strong asymmetry in GaAs samples indicates that the Si substrate thermal treatment preparation utilized is successful in achieving mostly double-steps for the vicinal substrate.

The sum of the four reflection intensities for GaSb grown on vicinal substrates is more than 50% higher than for GaAs grown on vicinal substrates (Figure 4.11(b)). This is evident when comparing the width of twin domains with (111) and $(\bar{1}\,\bar{1}\,1)$ habit planes in GaSb grown on nominal and vicinal Si substrates, which are about two times as wide as the respective in GaAs. This increase in the width of GaSb microtwins is visible in the $(1\,\bar{1}\,0)$ cross-sections of Figure 4.12(c) and (f), demonstrating an overall increase in the volume fraction of those twin variants. The width of twins in GaSb grown on nominal and vicinal Si substrates with two $(1\,\bar{1}\,1)$ and $(\bar{1}\,1\,1)$ habit planes are also about three times as wide as those in GaAs (the TEM images of the perpendicular [110] cross-section are not presented here).

5.3.2 Proposed Mechanism for Microtwin Reduction

The proposed mechanism for the reduction of microtwin volume is the transition to a step-flow growth mode induced by surface steps of vicinal substrates. On nominal oriented substrates, a transition to layer-by-layer growth simply allows for the continued propagation of nucleated epitaxial twins throughout the film as the growth front propagates normal to the substrate. It is highly possible that layer-by-layer growth is never achieved in some systems on nominal substrates, as is observed for InP and AlSb (Devenyi *et al*., 2011). On vicinal substrates, growth does not transition to a pure layer-by-layer growth mode, but instead to a step-flow growth mode, due to the surface steps present. From the transition point onwards, the growth front is not normal to the substrate

surface, but instead flows across the surface at an enhanced rate towards the tilt direction. This enhancement can also increase the fraction of twins forming in the step-flow direction, as is the case for GaAs grown on vicinal substrates. Growth fronts originating from the steps flow across the surface and overgrow islands that formed during the initial island growth mode. Since step-flow growth occurs down steps, towards the tilt direction, twins that were initially nucleated on habit planes away from the tilt direction during island growth are halted since they need to propagate opposite to the growth front. The transition from island to step-flow growth is evident due to the presence of nanotwins which propagate ~25 nm from the interface before termination, as is shown in the GaSb TEM DF image (Figure 4.13). This propagation distance into the film thickness is consistent with the transition from an island to step-flow growth mode as is apparent from the observed transition from a spotty to streaky RHEED pattern during the GaSb growth. The transition to step-flow growth ultimately decreases the propagation length, L from Eq. (5.1), of the twins with habit planes opposite to the tilt direction.

Greater vicinal angles are predicted to initiate step-flow growth from nucleation, and hence have the ability to completely eliminate twins opposite the tilt direction. Additionally, an offcut towards the [100] direction can induce surface steps in the two orthogonal <110> directions simultaneously (Fang *et al*., 1990), as shown in Figure 5.5. The two-dimensional cascade of a high density of surface steps that results is expected to decrease the twin density in two of four

{111} habit planes, reducing the overall intersections of microtwins that do so along incoherent interfaces.

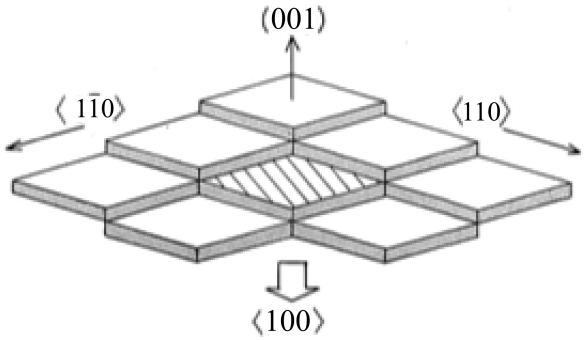

Figure 5.5: Schematic showing the effect of substrate surface misorientation of (001) tilted towards [100], which results in a two-dimensional array of surface steps in two orthogonal <110> directions, as adapted from (Kawabe & Ueda, 1987).

5.4 The Si(211) Solution

A ball and stick model (Figure 5.6) can be used to illustrate the 2.5° misorientation towards the $[\bar{1}\,1\,1]$ direction between the GaSb epilayer and the (211)-oriented Si substrate, as observed in the SAED pattern in Figure 4.17. This model of the GaSb/Si interface demonstrates the triple junction of the epitaxial orientation, twinned orientation, and the Si(211) surface. It can be seen from the simulated model, the Ga- and Sb-atoms in the twinned orientation are perfectly registered with the terrace and edge atoms of the Si substrate, respectively. More importantly, the +12.2% lattice mismatch between GaSb and Si is actually minimized to a mere -0.13% (in tension) in the twinned orientation. This is because the twinned orientation produces a variant that is [255]-oriented normal to the substrate, which results in {115} GaSb planes to be aligned with the $(\bar{1}\,1\,1)$ planes of the substrate. It can be surmised that this strain relief is the

driving force behind such unusual tilted epitaxy behaviour on Si(211) substrate. Recent work in the growth of group II-VI compound semiconductors on Si(211), such as that of CdTe and ZnTe, have reported similar tilts (3.5° and 2.66°, respectively) between the epilayer and substrate (Wang *et al*., 2011; Zhao, Jacobs, Jaime-Vasquez, Bubulac, & Smith, 2011). It can be further predicted that other cubic III-V compounds with a dissimilar lattice mismatch to Si will have a different degree of rotation.

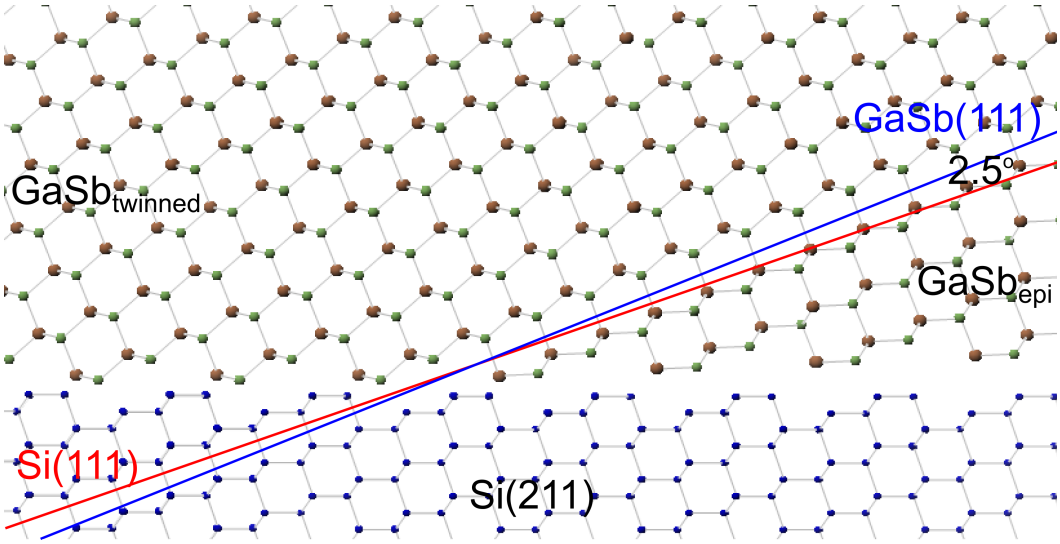

Figure 5.6: Ball and stick model of the GaSb/Si(211) interface, with twinned orientation on the left, and epitaxial orientation on the right separated by the (111) twin habit plane.

On the contrary, the same atomic registration of GaSb sublattices to the underlying Si substrate does not exist in the epitaxial variant. This correlates well with the jagged, misfit dislocation-like features observed at the GaSb/Si interface in the bright-field image of Figure 4.18(b), which was determined to be of the epitaxial orientation.

6. Conclusion and Future Work

Due to the highly lattice mismatched and heterovalent GaSb/Si interface, it is susceptible to a high density of structural defects, such as threading dislocations, stacking faults, microtwins, and anti-phase domains. The physical properties of such heteroepitaxial films are strongly dependent on the presence of extended defects that arise. Therefore it is crucial to understand the nature of these defects through an investigation using conventional transmission electron microscopy, and control the growth process to minimize their presence.

In this thesis, the presence of structural defects previously reported in literature within the GaSb/Si system are first confirmed, including threading and misfit dislocations, and microtwins. An extended study using the combined techniques of diffraction contrast imaging, (selected area) electron diffraction analysis, and two-dimensional X-ray diffraction has gained further insight to microtwins that arise during epitaxial growth. This includes an expanded understanding in the origin, propagation, distribution, as well as possible suppression of such epitaxial twins from a transition to step-flow growth mode. The presence anti-phase disorder is unambiguously observed with the use of superlattice diffraction contrast imaging, in conjunction with confirmation of a reversal of polarity using convergent beam electron diffraction analysis. A possible distinction between the dominant origin of anti-phase boundary formation in the heteroepitaxy of GaSb/Si and GaAs/Si has also been made.

Further effort was made to minimize the occurrences of anti-phase disorder through the use of vicinal (001)- and (211)-oriented Si substrates. The results showed promise that anti-phase disorder, such as the propagation of anti-phase boundaries can be controlled through the use of such substrates with a high density of surface steps. However, it must be taken into account the consequences of these surface steps in the other nucleation-induced defects, namely microtwins.

As part of the future work, the strain relief mechanism that is common in multiply twinned fcc and fcc-like crystal structures still requires more in-depth studies. The boundary in which the two second-order twins coincide is of particular interest, as observed in the GaSb epilayer grown in the absence of AlSb as buffer layer. Lastly, it is predicted that further increases to the vicinal offcut angle would reduce or even eliminate microtwins due to a pure step-flow growth mode, and offcuts towards the [100] direction would result in two-dimensional array of steps for the reduction of microtwins in two directions simultaneously. This type of asymmetric substrate surface is also expected to minimize the overall domain size of anti-phase domains, by inducing anti-phase boundaries of the self-annihilated nature to be confined close to the interface.

References

Akahane, K., Yamamoto, N., Gozu, S., & Ohtani, N. (2004). Heteroepitaxial growth of GaSb on Si(001) substrates. *Journal of Crystal Growth*, *264*(1-3), 21-25. doi:10.1016/j.jcrysgro.2003.12.041

Akahane, K., Yamamoto, N., Gozu, S., Ueta, A., & Ohtani, N. (2005). Initial growth stage of GaSb on Si(001) substrates with AlSb initiation layers. *Journal of Crystal Growth*, *283*(3-4), 297-302. doi:10.1016/j.jcrysgro.2005.06.001

Akahane, K., Yamamoto, N., Gozu, S., Ueta, A., & Ohtani, N. (2006). Residual carrier density in GaSb grown on Si substrates. *Thin Solid Films*, *515*(2), 748-751. doi:10.1016/j.tsf.2005.12.244

Balakrishnan, K., Feuillet, G., Ohta, K., Hamaguchi, H., Okumura, H., & Yoshida, S. (1997). Structural Analysis of Cubic GaN through X-Ray Pole Figure Generation. *Japanese Journal of Applied Physics*, *36*(Part 1, No. 10), 6221-6225. doi:10.1143/JJAP.36.6221

Brill, G., Chen, Y. P., Dhar, N. K., & Singh, R. (2003). Nucleation of ZnTe/CdTe epitaxy on high-miller-index Si surfaces. *Journal of Electronic Materials*, *32*(7), 717-722. doi:10.1007/s11664-003-0058-6

Bringans, R. D., Biegelsen, D. K., & Swartz, L. E. (1991). Atomic-step rearrangement on Si(001) by interaction with arsenic and the implication for GaAs-on-Si epitaxy. *Physical Review B*, *44*(7), 3054-3063.

Bringans, R. D., Olmstead, M. A., Ponce, F. A., Biegelsen, D. K., Krusor, B. S., & Yingling, R. D. (1988). The effect of a Ga prelayer on the beginning of GaAs epitaxy on Si. *Journal of Applied Physics*, *64*(7), 3472-3475.

Britten, J. F., & Guan, W. (2007). MAX3D - Visualization of Reciprocal Space Volumes. *Commission on Crystallographic Computing Newsletter*, *8*(8), 96.

Cahn, J. W. (1963). Hardening by spinodal decomposition. *Acta Metallurgica*, *11*(12), 1275-1282. doi:10.1016/0001-6160(63)90022-1

Chadi, D. J. (1987). Stabilities of Single-Layer and Bilayer Steps on Si(001) Surfaces. *Physical Review Letters*, *59*(15), 1691-1694.

Cho, N.-H., & Carter, C. B. (2001). Formation, faceting, and interaction behaviors of antiphase boundaries in GaAs thin films. *Journal of Materials Science*, *36*(17), 4209 - 4222. doi:10.1023/A:1017981324721

Cho, N.-H., De Cooman, B. C., Carter, C. B., Fletcher, R., & Wagner, D. K. (1985). Antiphase boundaries in GaAs. *Applied Physics Letters*, *47*(8), 879-881. doi:10.1063/1.95963

Cohen, D., & Carter, C. B. (2002). Structure of the (110) antiphase boundary in gallium phosphide. *Journal of Microscopy*, *208*(2), 84-99. doi:10.1046/j.1365-2818.2002.01070.x

Devenyi, G. A., Woo, S. Y., Ghanad-Tavakoli, S., Hughes, R. A., Kleiman, R. N., Botton, G. A., & Preston, J. S. (n.d.). The Role of Vicinal Silicon Surfaces in the Formation of Epitaxial Twins during the Growth of III-V Thin Films. *Submitted September 30, 2011 to Journal of Applied Physics*.

Dhar, N. K., Wood, C. E. C., Gray, A., Wei, H. Y., Salamanca-Riba, L., & Dinan, J. H. (1996). Heteroepitaxy of CdTe on {211} Si using crystallized amorphous ZnTe templates. *Journal of Vacuum Science & Technology B: Microelectronics and Nanometer Structures*, *14*(3), 2366. doi:10.1116/1.588862

Dhar, N. K., Zandian, M., Pasko, J. G., Arias, J. M., & Dinan, J. H. (1997). Planar p-on-n HgCdTe heterostructure infrared photodiodes on Si substrates by molecular beam epitaxy. *Applied Physics Letters*, *70*(13), 1730. doi:10.1063/1.118683

Edington, J. W. (1976). *Practical Electron Microscopy in Materials Science* (pp. 149-152). New York: Van Nostrand Reinhold Company.

Ernst, F., & Pirouz, P. (1989). The formation mechanism of planar defects in compound semiconductors grown epitaxially on {100} silicon substrates. *Journal of Materials Research*, *4*(4), 834-842. doi:10.1557/JMR.1989.0834

Fang, S. F., Adomi, K., Iyer, S., Morkoç, H., Zabel, H., Choi, C., & Otsuka, N. (1990). Gallium arsenide and other compound semiconductors on silicon. *Journal of Applied Physics*, *68*(7), R31-R58. doi:10.1063/1.346284

Fischer, R., Masselink, W. T., Klem, J., Henderson, T., McGlinn, T. C., Klein, M. V., Morkoç, H., et al. (1985). Growth and properties of GaAs/AlGaAs on nonpolar substrates using molecular beam epitaxy. *Journal of Applied Physics*, *58*(1), 374-381.

Georgakilas, A., Stoemenos, J., Tsagaraki, K., Komninou, P., Flevaris, N., Panayotatos, P., & Christou, A. (1993). Generation and annihilation of antiphase domain boundaries in GaAs on Si grown by molecular beam epitaxy. *Journal of Materials Research*, *8*(8), 1908-1921. doi:10.1557/JMR.1993.1908

Gottschalk, H., Patzer, G., & Alexander, H. (1978). Stacking fault energy and ionicity of cubic III–V compounds. *Physica Status Solidi (a)*, *45*(1), 207-217. doi:10.1002/pssa.2210450125

Gowers, J. P. (1984). TEM image contrast from antiphase domains in GaAs: Ge(001) grown by MBE. *Applied Physics A Solids and Surfaces*, *34*(4), 231-236. doi:10.1007/BF00616577

Guelton, N., Saint-Jacques, R. G., Lalande, G., & Dodelet, J.-P. (1995). Microstructural study of GaAs epitaxial layers on Ge(100) substrates. *Journal of Materials Research*, *10*(4), 843-852. doi:10.1557/JMR.1995.0843

Holt, D. B. (1969). Antiphase boundaries in semiconducting compounds. *Journal of Physics and Chemistry of Solids*, *30*(6), 1297-1308. doi:10.1016/0022-3697(69)90191-7

Holt, D. B., & Yacobi, B. G. (2007). *Extended Defects in Semiconductors: Electronic Properties, Device Effects and Structures*. Cambridge University Press.

Hornstra, J. (1959). Models of grain boundaries in the diamond lattice I. Tilt about <110> *Physica*, *25*(1-6), 409-422. doi:10.1016/S0031-8914(59)94454-4

Huang, S. H., Balakrishnan, G., Khoshakhlagh, a, Dawson, L. R., & Huffaker, D. L. (2008). Simultaneous interfacial misfit array formation and antiphase domain suppression on miscut silicon substrate. *Applied Physics Letters*, *93*(7), 071102. doi:10.1063/1.2970997

Hudait, M. K., & Krupanidhi, S. B. (2000). Transmission electron microscopic study of GaAs/Ge heterostructures grown by low-pressure metal organic vapor phase epitaxy. *Materials Research Bulletin*, *35*(1), 125-133. doi:10.1016/S0025-5408(00)00191-4

Ino, S. (1966). Epitaxial Growth of Metals on Rocksalt Faces Cleaved in Vacuum. II. Orientation and Structure of Gold Particles Formed in Ultrahigh Vacuum. *Journal of the Physical Society of Japan*, *21*(2), 346-362. doi:10.1143/JPSJ.21.346

Ino, S., & Ogawa, S. (1967). Multiply Twinned Particles at Earlier Stages of Gold Film Formation on Alkalihalide Crystals. *Journal of the Physical Society of Japan*, *22*(6), 1365-1374. doi:10.1143/JPSJ.22.1365

Ishizuka, K., & Taftø, J. (1984). Quantitative analysis of CBED to determine polarity and ionicity of ZnS-type crystals. *Acta Crystallographica Section B Structural Science*, *40*(4), 332-337. doi:10.1107/S010876818400224X

Kawabe, M., & Ueda, T. (1987). Self-Annihilation of Antiphase Boundary in GaAs on Si(100) Grown by Molecular Beam Epitaxy. *Japanese Journal of Applied Physics*, *26*(6), L944-L946. doi:10.1143/JJAP.26.L944

Kim, Y. H., Lee, J. Y., Noh, Y. G., Kim, M. D., Cho, S. M., Kwon, Y. J., & Oh, J. E. (2006). Growth mode and structural characterization of GaSb on Si (001) substrate: A transmission electron microscopy study. *Applied Physics Letters*, *88*(24), 241907. doi:10.1063/1.2209714

Kiyota, Y., & Inada, T. (2001). Sticking coefficient of boron and phosphorus on silicon during vapor-phase doping. *Journal of Vacuum Science & Technology A: Vacuum, Surfaces, and Films*, *19*(5), 2441. doi:10.1116/1.1387055

Komninou, P., Stoemenos, J., Dimitrakopulos, G. P., & Karakostas, T. (1994). Misfit dislocations and antiphase domain boundaries in GaAs/Si interface. *Journal of Applied Physics*, *75*(1), 143-152. doi:10.1063/1.355903

Komoda, T. (1968). Study on the Structure of Evaporated Gold Particles by Means of a High Resolution Electron Microscope. *Japanese Journal of Applied Physics*, *7*(1), 27-30. doi:10.1143/JJAP.7.27

Kroemer, H. (1983). Heterostructure devices: A device physicist looks at interfaces. *Surface Science*, *132*(1-3), 543-576. doi:10.1016/0039-6028(83)90561-7

Kroemer, H. (1987). Polar-on-nonpolar epitaxy. *Journal of Crystal Growth*, *81*(1-4), 193-204. doi:10.1016/0022-0248(87)90391-5

Kubiak, R. A. A. (1985). Enhanced sticking coefficients and improved profile control using boron and antimony as coevaporated dopants in Si–MBE. *Journal of Vacuum Science & Technology B: Microelectronics and Nanometer Structures*, *3*(2), 592. doi:10.1116/1.583142

Li, Y., & Giling, L. J. (1996). A closer study on the self-annihilation of antiphase boundaries in GaAs epilayers. *Journal of Crystal Growth*, *163*, 203-211.

Li, Y., Salviati, G., Bongers, M. M. G., Lazzarini, L., Nasi, L., & Giling, L. J. (1996). On the formation of antiphase domains in the system of GaAs on Ge. *Journal of Crystal Growth*, *163*(3), 195-202. doi:10.1016/0022-0248(95)00958-2

Li, Y., Lazzarini, L., Giling, L. J., & Salviati, G. (1994). On the sublattice location of GaAs grown on Ge. *Journal of Applied Physics*, *76*(10), 5748-5753. doi:10.1063/1.358412

Liliental-Weber, Z., Weber, E. R., Parechanian-Allen, L., & Washburn, J. (1988). On the use of Convergent-Beam Electron Diffraction for Identification of Antiphase Boundaries in GaAs grown on Si. *Ultramicroscopy*, *26*, 59-63.

Loretto, M. H. (1994). *Electron Beam Analysis of Materials* (2nd ed., pp. 172-182). London: Chapman & Hall.

Malik, R. J., van der Ziel, J. P., Levine, B. F., Bethea, C. G., & Walker, J. (1986). Molecular-beam epitaxy of GaSb/AlSb optical device layers on Si(100). *Journal of Applied Physics*, *59*(11), 3909-3911. doi:10.1063/1.336734

Morizane, K. (1977). Antiphase domain structures in GaP and GaAs epitaxial layers grown on Si and Ge. *Journal of Crystal Growth*, *38*, 249-254.

Neave, J. H., Larsen, P. K., Joyce, B. A., Gowers, J. P., & van der Veen, J. F. (1983). Some observations on Ge:GaAs(001) and GaAs:Ge(001) interfaces and films. *Journal of Vacuum Science & Technology B: Microelectronics and Nanometer Structures*, *1*(3), 668-674. doi:10.1116/1.582574

Neergaard Waltenburg, H., & Yates, J. T. (1995). Surface Chemistry of Silicon. *Chemical Reviews*, *95*(5), 1589-1673. doi:10.1021/cr00037a600

Neumann, D. A., Zabel, H., Fischer, R., & Morkoç, H. (1987). Structural properties of GaAs on (001) oriented Si and Ge substrates. *Journal of Applied Physics*, *61*(3), 1023-1029. doi:10.1063/1.338192

Neumann, D. A., Zhu, X., Zabel, H., Henderson, T., Fischer, R., Masselink, W. T., Klem, J., et al. (1986). Structural properties of GaAs on Si and Ge substrates. *Journal of Vacuum Science & Technology B: Microelectronics and Nanometer Structures*, *4*(2), 642-644. doi:10.1116/1.583585

Noh, Y. K., Park, S. R., Kim, M. D., Kwon, Y. J., Oh, J. E., Kim, Y. H., Lee, J. Y., et al. (2007). Growth mechanisms and structural properties of self-assembled AlSb quantum dots on a Si(100) substrate. *Journal of Crystal Growth*, *301-302*, 244-247. doi:10.1016/j.jcrysgro.2006.11.187

Oda, O. (2007). *Compound Semiconductor Bulk Materials and Characterizations* (p. 556). Singapore: World Scientific.

Parkinson, P., Joyce, H. J., Gao, Q., Tan, H. H., Zhang, X., Zou, J., Jagadish, C., et al. (2009). Carrier lifetime and mobility enhancement in nearly defect-free core-shell nanowires measured using time-resolved terahertz spectroscopy. *Nano letters*, *9*(9), 3349-53. doi:10.1021/nl9016336

Pehlke, E., & Tersoff, J. (1991). Phase diagram of vicinal Si (001) surfaces. *Physical Review Letters*, *67*(10), 1290-1293. Retrieved from http://link.aps.org/doi/10.1103/PhysRevLett.67.1290

Posthill, J. B., Tam, J. C. L., Das, K., Humphreys, T. P., & Parikh, N. R. (1988). Observation of antiphase domain boundaries in GaAs on silicon by transmission electron microscopy. *Applied Physics Letters*, *53*(13), 1207-1209.

Rao, S. R., Shintri, S. S., & Bhat, I. B. (2009). Metalorganic Vapor-Phase Epitaxial Growth of (211)B CdTe on (211) Si Using Ge Interfacial Layer. *Journal of Electronic Materials*, *38*(8), 1618-1623. doi:10.1007/s11664-009-0719-1

Rubel, O., & Baranovskii, S. D. (2009). Formation energies of antiphase boundaries in GaAs and GaP: An ab Initio study. *International Journal of Molecular Sciences*, *10*(12), 5104-5114. doi:10.3390/ijms10125104

Sakamoto, T., & Hashiguchi, G. (1986). Si (001)-2×1 Single-Domain Structure Obtained by High Temperature Annealing. *Japanese Journal of Applied Physics*, *25*(1), L78-L80. doi:10.1143/JJAP.25.L78

Schroder-Bergen, E., & Ranke, W. (1991). Steps on Si (001) vicinal surfaces tilted by various angles in the [1-10]-, [100]- and [2-10]-zones, investigated by high-resolution LEED. *Surface Science*, *259*, 323-338.

Spiecker, E. (2002). Determination of crystal polarity from bend contours in transmission electron microscope images. *Ultramicroscopy*, *92*(3-4), 111-132. Retrieved from http://linkinghub.elsevier.com/retrieve/pii/S0304399102000724

Stowell, M. J. (1975). Defects in Epitaxial Deposits. In J. W. Matthews (Ed.), *Epitaxial Growth. Part B* (pp. 470-474). New York: Academic Press.

Taftø, J., & Spence, J. C. H. (1982). A simple method for the determination of structure-factor phase relationships and crystal polarity using electron diffraction. *Journal of Applied Crystallography*, *15*(1), 60-64. doi:10.1107/S0021889882011352

Tersoff, J., van der Gon, A. W. D., & Tromp, R. (1994). Critical island size for layer-by-layer growth. *Physical Review Letters*, *72*(2), 266-269. doi:10.1103/PhysRevLett.72.266

Ueda, O., Soga, T., Jimbo, T., & Umeno, M. (1989). Direct evidence for self-annihilation of antiphase domains in GaAs/Si heterostructures. *Applied Physics Letters*, *55*(5), 445-447.

van Landuyt, J. (1966). Determination of the Displacement Vector at the Anti-Phase Boundaries in Rutile by Contrast Experiments in the Electron Microscope. *physica status solidi (b)*, *16*(2), 585-590. doi:10.1002/pssb.19660160225

Uppal, P. N., & Kroemer, H. (1985). Molecular beam epitaxial growth of GaAs on Si(211). *Journal of Applied Physics*, *58*(6), 2195-2203.

Vajargah, S. H., Couillard, M., Cui, K., Tavakoli, S. G., Robinson, B. J., Kleiman, R. N., Preston, J. S., et al. (2011). Strain relief and AlSb buffer layer morphology in GaSb heteroepitaxial films grown on Si as revealed by high-angle annular dark-field scanning transmission electron microscopy. *Applied Physics Letters*, *98*(8), 082113. doi:10.1063/1.3551626

Wagner, C. N. J. (1966). Analysis of the broadening and changes in position of peaks in an X-ray powder pattern. In J. B. Cohen & J. E. Hilliard (Eds.), *Local Atomic Arrangements Studied by X-Ray Diffraction* (pp. 224-225). Gordon and Breach.

Wang, X. J., Chang, Y., Becker, C. R., Grein, C. H., Sivananthan, S., & Kodama, R. (2011). Microstructure of Heteroepitaxial ZnTe Grown by Molecular

Beam Epitaxy on Si(211) Substrates. *Journal of Electronic Materials*, *40*(8), 1860-1866. doi:10.1007/s11664-011-1648-3

Wei, X. L., & Aindow, M. (1994). Development of anisotropic microtwin distributions in GaAs grown on 4°-off (001) Si by molecular beam epitaxy. *Applied Physics Letters*, *65*(15), 1903-1905. doi:10.1063/1.112834

Williams, D. B., & Carter, C. B. (2009). *Transmission Electron Microscopy A Textbook for Materials Science* (2nd ed.). Boston, MA: Springer US. doi:10.1007/978-0-387-76501-3

Xie, Q. H., Fung, K. K., Ding, A. J., Cai, L. H., Huang, Y., & Zhou, J. M. (1990). Asymmetric distribution of microtwins in a GaAs/Si heterostructure grown by molecular beam epitaxy. *Applied Physics Letters*, *57*(26), 2803-2805. doi:10.1063/1.103792

Zhao, W. F., Jacobs, R. N., Jaime-Vasquez, M., Bubulac, L. O., & Smith, D. J. (2011). Microstructural Characterization of CdTe(211)B/ZnTe/Si(211) Heterostructures Grown by Molecular Beam Epitaxy. *Journal of Electronic Materials*, *40*(8), 1733-1737. doi:10.1007/s11664-011-1673-2